Chapter 1

Shell-correction and orbital-free density-functional methods for finite systems

Constantine Yannouleas[*] and Uzi Landman[†]

School of Physics, Georgia Institute of Technology, Atlanta, Georgia 30332-0430, USA

Orbital-free (OF) methods promise significant speed-up of computations based on density functional theory (DFT). In this field, the development of accurate kinetic-energy density functionals remains an open question. In this chapter we review the shell-correction method (SCM, commonly known as Strutinsky's averaging method) applied originally in nuclear physics and its more recent formulation in the context of DFT [Yannouleas and Landman, *Phys. Rev. B* **48**, 8376 (1993)]. We demonstrate the DFT-SCM method through its earlier applications to condensed-matter finite systems, including metal clusters, fullerenes, and metal nanowires. The DFT-SCM incorporates quantum mechanical interference effects and thus offers an improvement compared to the use of Thomas-Fermi-type kinetic energy density functionals in OF-DFT.

1.1. Introduction

1.1.1. *Preamble*

Often theoretical methods (in particular computational techniques) are developed in response to emerging scientific challenges in specific fields. The development of the shell correction method (SCM) by Strutinsky in the late 1960's [1] was motivated by the observation of large nonuniformities (oscillatory behavior) exhibited by a number of nuclear properties as a function of the nuclear size. These properties included: total nuclear masses, nuclear deformation energies, and large distortions and fission barriers. While it was understood already that the total energy of nuclei can be decomposed into an oscillatory part and one that shows a slow "smooth" variation as a function of size, Strutinsky's seminal contribution was to calculate the two parts from different nuclear models: the former from the nuclear shell model and the latter from the liquid drop model. In particular, the calculation of the oscillatory part was enabled by employing an averaging method that smeared the single particle spectrum associated with a nuclear model potential. It is recognized that the Strutinsky procedure provides a method which "reproduces microscopic

[*]Constantine.Yannouleas@physics.gatech.edu
[†]Uzi.Landman@physics.gatech.edu

2   *Constantine Yannouleas and Uzi Landman*

results in an optimal way using phenomenological models" [2]; in the Appendix
we describe an adaptation of the Strutinsky phenomenological procedure to metal
clusters; we term this procedure as the semi-empirical (SE)-SCM.

In this chapter, we focus on our development in the early 1990's of the micro-
scopic density-functional-theory (DFT)-SCM approach [3], where we have shown
that the total energy of a condensed-matter finite system can be identified with
the Harris functional [see Eq. (1.16)], with the shell correction [Eq. (1.23)] being
expressed through both the kinetic energy, T_{sh}, of this functional [Eq. (1.19)] and
the kinetic energy of an extended-Thomas-Fermi (ETF) functional expanded to
fourth-order density gradients [see T_{ETF} in Eq. (1.22)]. It is important to note that
in our procedure an optimized input density is used in the Harris functional. This
optimization can be achieved through a variational procedure [using an orbital-free
(OF) energy functional, e.g., the ETF functional with 4th-order gradients] with
a parametrized trial density profile [see Eq. (1.25)], or through the use [see Eq.
(1.24)] of the variational principle applied to an orbital-free energy functional. (For
literature regarding orbital-free kinetic-energy functionals, see, e.g., Refs. [4–9].) A
similar optimization of an OF/4th-order-ETF density has been shown to be con-
sistent with the Strutinsky averaging approach [10]. Such 4th-order optimization
of the input density renders rather ambiguous any direct (term-by-term) compari-
son between the method proposed by us and subsequent treatments, which extend
the DFT-SCM to include higher-order shell-correction terms without input-density
optimization [11, 12] (see also Ref. [13]). Indeed, the input-density optimization
(in particular with the use of 4th-order gradients) minimizes contributions from
higher-order shell corrections.

In light of certain existing similarities between the physics of nuclei and clusters
(despite the large disparity in spatial and energy scales and the different origins of
inter-particle interactions in these systems), in particular the finding of electronic
shell effects in clusters [14–18], it was natural to use the jellium model in the early
applications of the DFT-SCM to clusters. However, as noted [3] already early on,
"the very good agreement between our results and those obtained via Kohn-Sham
self-consistent jellium calculations suggested that it would be worthwhile to extend
the application of our method to more general electronic structure calculations ex-
tending beyond the jellium model, where the trial density used for minimization of
the ETF functional could be taken as a superposition of site densities, as in the
Harris method." Additionally, generalization of the DFT-SCM method to calcu-
lations of extended (bulk and surface) systems appeared rather natural. Indeed,
recent promising applications of DFT-SCM in this spirit have appeared [19, 20]. In
this case, the term "shell correction effects" is also maintained, although "quantum
interference effects" could be more appropriate for extended systems.

1.1.2. *Motivation for finite systems*

One of the principle themes in research on finite systems (e.g., nuclei, atomic and molecular clusters, and nano-structured materials) is the search for size-evolutionary patterns (SEPs) of properties of such systems and elucidation of the physical principles underlying such patterns [21].

Various physical and chemical properties of finite systems exhibit SEPs, including:

1. Structural characteristics pertaining to atomic arrangements and particle morphologies and shapes;
2. Excitation spectra involving bound-bound transitions, ionization potentials (IPs), and electron affinities (EAs);
3. Collective excitations (electronic and vibrational);
4. Magnetic properties;
5. Abundance spectra and stability patterns, and their relation to binding and cohesion energetics, and to the pathways and rates of dissociation, fragmentation, and fission of charged clusters;
6. Thermodynamic stability and phase changes;
7. Chemical reactivity.

The variations with size of certain properties of materials aggregates are commonly found to scale on the average with the surface to volume ratio of the cluster, i.e., $S/\Omega \sim R^{-1} \sim N^{1/3}$, where S, Ω, R, and N are the surface area, volume, average radius, and number of particles, respectively (the physical origins of such scaling may vary for different properties). In general, the behavior of SEPs in finite systems in terms of such scaling is non-universal, in the sense that it is non-monotonic exhibiting characteristic discontinuities. Nevertheless, in many occasions, it is convenient to analyze the energetics of finite systems in terms of two contributions, namely, (i) a term which describes the energetics as a function of the system size in an average sense (not including shell-closure effects), referrred to usually as describing the "smooth" part of the size dependence, and (ii) an electronic shell-correction term. The first term is the one which is expected to vary smoothly and be expressible as an expansion in S/Ω, while the second one contains the characteristic oscillatory patterns as the size of the finite system is varied. Such a strategy has been introduced [1] and often used in studies of nuclei [2, 22], and has been adopted recently for investigations of metal clusters [3, 23–38], fullerenes [39], and metal nanowires [40–42]. As a motivating example, we show in Fig. 1.1 the SEP of the IPs of Na_N clusters, which illustrates odd-even oscillations in the observed spectrum, a smooth description of the pattern [Fig. 1.1(a)], and two levels of shell-corrected descriptions — one assuming spherical symmetry [Fig. 1.1(b)], and the other allowing for triaxial shape deformations [Fig. 1.1(c)]. The progressive improvement of the level of agreement between the experimental and theoretical patterns is evident.
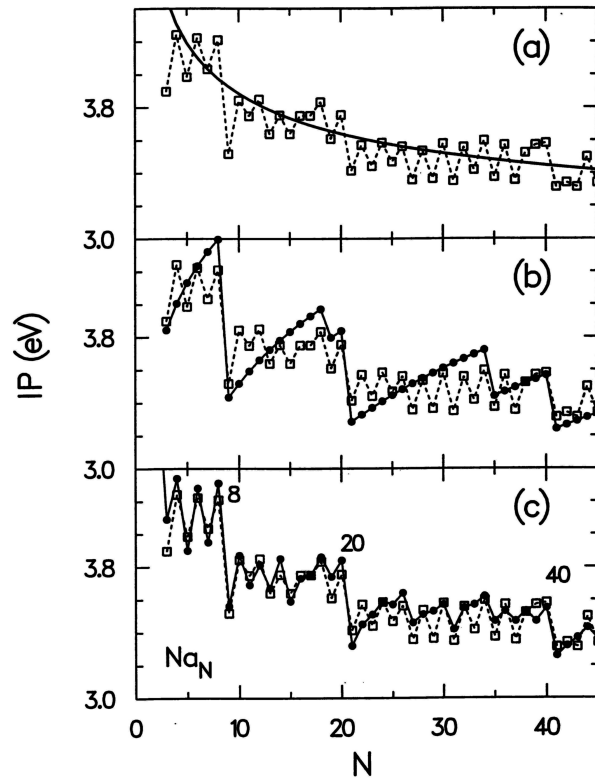
Constantine Yannouleas and Uzi Landman

Fig. 1.1.   Ionization potentials of Na$_N$ clusters. Open squares: Experimental measurements of Refs. [15, 17]. The solid line at the top panel (a) represents the smooth contribution to the theoretical total IPs. The solid circles in the middle (b) and bottom (c) panels are the total SCM IPs. The shapes of sodium clusters have been assumed spherical in the middle panel, while triaxial deformations have been considered at the bottom one.

1.1.3. *Plan of the chapter*

The chapter is organized as follows:

In Sec. 1.2, the general methodology of shell-correction methods is reviewed, and the microscopic DFT-SCM is introduced and presented in detail in Sec. 1.2.2.

Applications of the DFT-SCM to condensed-matter finite systems are presented in Sec. 1.3 for three different characteristic nanosystems, namely, metal clusters (Sec. 1.3.1), charged fullerenes (Sec. 1.3.2), and metallic nanowires (Sec. 1.3.3).

In the Appendix, we describe the semiempirical SCM for clusters, which is closer to the spirit of Strutinsky's original phenomenological approach for nuclei. There we also briefly present applications of the SE-SCM to triaxial shape deformations and fission of metal clusters.

A summary is given in Sec. 1.4.

1.2. Methodology and derivation of microscopic DFT-SCM

1.2.1. *Historical review of SCM*

It has long been recognized in nuclear physics that the dependence of ground-state properties of nuclei on the number of particles can be viewed as the sum of two contributions: the first contribution varies smoothly with the particle number (number of protons N_p and neutrons N_n) and is referred to as the *smooth* part; the second contribution gives a superimposed structure on the smooth curve and exhibits an oscillatory behavior, with extrema at the nuclear magic numbers [22, 43].

Nuclear masses have provided a prototype for this behavior [43]. Indeed, the main contributions to the experimental nuclear binding energies are smooth functions of the number of protons and neutrons, and are described by the semi-empirical mass formula [44, 45]. The presence of these smooth terms led to the introduction of the liquid-drop model (LDM), according to which the nucleus is viewed as a drop of a nonviscous fluid whose total energy is specified by volume, surface, and curvature contributions [22, 43, 46].

The deviations of the binding energies from the smooth variation implied by the LDM have been shown [1, 46] to arise from the shell structure associated with the bunching of the discrete single-particle spectra of the nucleons, and are commonly referred to as the shell correction. Substantial progress in our understanding of the stability of strongly deformed open-shell nuclei and of the dynamics of nuclear fission was achieved when Strutinsky proposed [1] a physically motivated efficient way of calculating the shell corrections. The method consists of averaging [see the Appendix, Eq. (A.1) and Eq. (A.2)] the single-particle spectra of phenomenological deformed potentials and of subtracting the ensuing average from the total sum of single-particle energies.

While certain analogies, portrayed in experimental data, between properties of nuclei and elemental clusters have been recognized, the nuclear-physics approach of separating the various quantities as a function of size into a smooth part and a shell correction part has only partially been explored in the case of metal clusters. In particular, several investigations [47–50] had used the ETF method in conjunction with the jellium approximation to determine the average (smooth, in the sense defined above) behavior of metal clusters, but had not pursued a method for calculating the shell corrections.

In the absence of a method for appropriately calculating shell-corrections for metal clusters in the context of the semiclassical ETF method, it had been presumed that the ETF method was most useful for larger clusters, since the shell effects diminish with increasing size. Indeed, several studies had been carried out with this method addressing the asymptotic behavior of ground-state properties towards the behavior of a jellium sphere of infinite size [51, 52].

It has been observed [48, 53–56], however, that the single-particle potentials resulting from the semiclassical method are very close, even for small cluster sizes,

6   *Constantine Yannouleas and Uzi Landman*

to those obtained via self-consistent solution of the local density functional approximation (LDA) using the Kohn-Sham (KS) equations [57]. These semiclassical potentials were used extensively to describe the optical (linear) response of spherical metal clusters, for small [53–55], as well as larger sizes [56] (for an experimental review on optical properties, cf. Refs. [58, 59]). The results of this approach are consistent with time-dependent local density functional approximation (TDLDA) calculations which use the KS solutions [60, 61].

It is natural to explore the use of these semiclassical potentials, in the spirit of Strutinsky's approach, for evaluation of shell corrections in metal clusters of arbitrary size. Below we describe a microscopic derivation of an SCM in conjunction with the density functional theory [3, 23, 24], and its applications in investigations of the properties of metal clusters and fullerenes. Particularly interesting and promising is the manner by which the shell corrections are introduced by us at the microscopic level through the kinetic energy term [3, 23, 24], instead of the traditional semiempirical Strutinsky averaging procedure of the single-particle spectrum [1, 31]. In particular, our approach leads to an energy functional that corrects many shortcomings of the orbital-free DFT, and one that is competitive in numerical accuracy and largely advantageous in computational speed compared to the KS method.

1.2.2. *DFT-SCM*

Underlying the development of the shell-correction method is the idea of approximating the total energy $E_{\text{total}}(N)$ of a finite interacting fermion system as

$$E_{\text{total}}(N) = \widetilde{E}(N) + \Delta E_{sh}(N), \tag{1.1}$$

where $\widetilde{E}$ is the part that varies smoothly as a function of system size, and ΔE_{sh} is an oscillatory term. Various implementations of such a separation consist of different choices and methods for evaluating the two terms in Eq. (1.1). Before discussing such methods, we outline a microscopic derivation of Eq. (1.1).

Motivated by the behavior of the empirical nuclear binding energies, Strutinsky conjectured that the self-consistent Hartree-Fock density ρ_{HF} can be decomposed into a smooth density $\widetilde{\rho}$ and a fluctuating contribution $\delta\rho$, namely $\rho_{HF} = \widetilde{\rho} + \delta\rho$. Then, he proceeded to show that, to second-order in $\delta\rho$, the Hartree-Fock energy is equal to the result that the same Hartree-Fock expression yields when ρ_{HF} is replaced by the smooth density $\widetilde{\rho}$ and the Hartree-Fock single-particle energies ε_i^{HF} are replaced by the single-particle energies corresponding to the smooth potential constructed with the smooth density $\widetilde{\rho}$. Namely, he showed that

$$E_{HF} = E_{Str} + O(\delta\rho^2), \tag{1.2}$$

where the Hartree-Fock electronic energy is given by the expression

$$E_{HF} = \sum_{i=1}^{\text{occ}} \varepsilon_i^{HF} - \frac{1}{2} \int d\mathbf{r}d\mathbf{r}' \mathcal{V}(\mathbf{r} - \mathbf{r}')[\rho_{HF}(\mathbf{r}, \mathbf{r})\rho_{HF}(\mathbf{r}', \mathbf{r}') - \rho_{HF}(\mathbf{r}, \mathbf{r}')^2], \tag{1.3}$$

with ε_i^{HF} being the eigenvalues obtained through a self-consistent solution of the HF equation,

$$\left(-\frac{\hbar^2}{2m}\nabla^2 + U_{HF}\right)\phi_i = \varepsilon_i^{HF}\phi_i, \tag{1.4}$$

where

$$U_{HF}(\mathbf{r})\phi_i(\mathbf{r}) = \int d\mathbf{r}'\mathcal{V}(\mathbf{r}-\mathbf{r}')[\rho_{HF}(\mathbf{r}',\mathbf{r}')\phi_i(\mathbf{r}) - \rho_{HF}(\mathbf{r}',\mathbf{r})\phi_i(\mathbf{r}')]. \tag{1.5}$$

The Strutinsky approximate energy is written as follows,

$$E_{Str} = \sum_{i=1}^{\text{occ}} \widetilde{\varepsilon}_i - \frac{1}{2}\int d\mathbf{r}d\mathbf{r}'\mathcal{V}(\mathbf{r}-\mathbf{r}')[\widetilde{\rho}(\mathbf{r},\mathbf{r})\widetilde{\rho}(\mathbf{r}',\mathbf{r}') - \widetilde{\rho}(\mathbf{r},\mathbf{r}')^2], \tag{1.6}$$

where the index i in Eq. (1.3) and Eq. (1.6) runs only over the occupied states (spin degeneracy is naturally implied). The single-particle energies $\widetilde{\varepsilon}_i$ correspond to a smooth potential $\widetilde{U}$. Namely, they are eigenvalues of a Schrödinger equation,

$$\left(-\frac{\hbar^2}{2m}\nabla^2 + \widetilde{U}\right)\varphi_i = \widetilde{\varepsilon}_i\varphi_i, \tag{1.7}$$

where the smooth potential $\widetilde{U}$ depends on the smooth density $\widetilde{\rho}$, i.e.,

$$\widetilde{U}(\mathbf{r})\varphi_i(\mathbf{r}) = \int d\mathbf{r}'\mathcal{V}(\mathbf{r}-\mathbf{r}')[\widetilde{\rho}(\mathbf{r}',\mathbf{r}')\varphi_i(\mathbf{r}) - \widetilde{\rho}(\mathbf{r}',\mathbf{r})\varphi_i(\mathbf{r}')], \tag{1.8}$$

and $\mathcal{V}$ is the nuclear two-body interaction potential.

It should be noted that while Eq. (1.6)− Eq. (1.8) look formally similar to the Hartree-Fock equations (1.3-1.5), their content is different. Specifically, while in the HF equations, the density ρ_{HF} is self-consistent with the wavefunction solutions of Eq. (1.4), the density $\widetilde{\rho}$ in Eq. (1.6)− Eq. (1.8) is not self-consistent with the wavefunction solutions of the corresponding single-particle Eq. (1.7), i.e., $\widetilde{\rho} \neq \sum_{i=1}^{\text{occ}} |\varphi_i|^2$. We return to this issue below.

Since the second term in Eq. (1.6) is a smooth quantity, Eq. (1.2) states that all shell corrections are, to first order in $\delta\rho$, contained in the sum of the single-particle energies $\sum_{i=1}^{\text{occ}}\widetilde{\varepsilon}_i$. Consequently, Eq. (1.6) can be used as a basis for a separation of the total energy into smooth and shell-correction terms as in Eq. (1.1). Indeed Strutinsky suggested a semi-empirical method of such separation through an averaging procedure of the single-particle energies $\widetilde{\varepsilon}_i$ in conjunction with a phenomenological (or semi-empirical) model [the liquid drop model (LDM)] for the smooth part (see the appendix).

Motivated by the above considerations, we have extended them [3, 23, 24] in the context of density functional theory for electronic structure calculations. First we review pertinent aspects of the DFT theory. In DFT, the total energy is given by

$$E[\rho] = T[\rho] + \int\left\{\left[\frac{1}{2}V_H[\rho(\mathbf{r})] + V_I(\mathbf{r})\right]\rho(\mathbf{r})\right\}d\mathbf{r} + \int\mathcal{E}_{xc}[\rho(\mathbf{r})]d\mathbf{r} + E_I, \tag{1.9}$$

Constantine Yannouleas and Uzi Landman

where V_H is the Hartree repulsive potential among the electrons, V_I is the interaction potential between the electrons and ions, $\mathcal{E}_{xc}$ is the exchange-correlation functional [the corresponding xc potential is given as $V_{xc}(\mathbf{r}) \equiv \delta \mathcal{E}_{xc} \rho(\mathbf{r})/\delta \rho(\mathbf{r})$] and $T[\rho]$ is given in terms of a yet unknown functional $t[\rho(\mathbf{r})]$ as $T[\rho] = \int t[\rho(\mathbf{r})]d\mathbf{r}$. E_I is the interaction energy of the ions.

In the Kohn-Sham (KS)-DFT theory, the electron density is evaluated from the single-particle wave functions $\phi_{KS,i}(\mathbf{r})$ as

$$\rho_{KS}(\mathbf{r}) = \sum_{i=1}^{\text{occ}} |\phi_{KS,i}(\mathbf{r})|^2, \tag{1.10}$$

where $\phi_{KS,i}(\mathbf{r})$ are obtained from a self-consistent solution of the KS equations,

$$\left[-\frac{\hbar^2}{2m} \nabla^2 + V_{KS} \right] \phi_{KS,i}(\mathbf{r}) = \varepsilon_{KS,i} \phi_{KS,i}(\mathbf{r}) \tag{1.11}$$

where

$$V_{KS}[\rho_{KS}(\mathbf{r})] = V_H[\rho_{KS}(\mathbf{r})] + V_{xc}[\rho_{KS}(\mathbf{r})] + V_I(\mathbf{r}). \tag{1.12}$$

The kinetic energy term in Eq. (1.9) is given by

$$T[\rho_{KS}] = \sum_{i=1}^{\text{occ}} < \phi_{KS,i}| -\frac{\hbar^2}{2m} \nabla^2 |\phi_{KS,i} >, \tag{1.13}$$

which can also be written as

$$T[\rho_{KS}] = \sum_{i=1}^{\text{occ}} \varepsilon_{KS,i} - \int \rho_{KS}(\mathbf{r}) V_{KS}[\rho_{KS}(\mathbf{r})]d\mathbf{r}. \tag{1.14}$$

According to the Hohenberg-Kohn theorem, the energy functional (1.9) is a minimum at the true ground density ρ_{gs}, which in the context of the KS-DFT theory corresponds the the density, ρ_{KS}, obtained from an iterative self-consistent solution of Eq. (1.11). In other words, combining Eq. (1.9) and Eq. (1.14), and denoting by "in" and "out" the trial and output densities of an iteration cycle in the solution of the KS equation [Eq. (1.11)], one obtains,

$$E_{KS}[\rho_{KS}^{\text{out}}] = E_I + \sum_{i=1}^{\text{occ}} \varepsilon_{KS,i}^{\text{out}} +$$

$$\int \left\{ \frac{1}{2} V_H[\rho_{KS}^{\text{out}}(\mathbf{r})] + \mathcal{E}_{xc}[\rho_{KS}^{\text{out}}(\mathbf{r})] + V_I(\mathbf{r}) \right\} \rho_{KS}^{\text{out}}(\mathbf{r})d\mathbf{r} -$$

$$\int \rho_{KS}^{\text{out}}(\mathbf{r}) V_{KS}[\rho_{KS}^{\text{in}}(\mathbf{r})]d\mathbf{r}. \tag{1.15}$$

Note that the expression on the right involves both ρ_{KS}^{out} and ρ_{KS}^{in}. Self-consistency is achieved when $\delta \rho_{KS}^{\text{out,in}}(\mathbf{r}) = \rho_{KS}^{\text{out}}(\mathbf{r}) - \rho_{KS}^{\text{in}}(\mathbf{r})$ becomes arbitrarily small (i.e., when ρ_{KS}^{out} converges to ρ_{KS}).

On the other hand, it is desirable to introduce approximate energy functionals for the calculations of ground-state electronic properties, providing simplified, yet

accurate, computational schemes. It is indeed possible to construct such functionals [62–66], an example of which was introduced by J. Harris [62], where self-consistency is circumvented and the result is accurate to second order in the difference between the trial and the self-consistent KS density (see in particular Eq. (24a) of Ref. [66]; the same also holds true for the difference between the trial and the output densities of the Harris functional).

The expression of the Harris functional is obtained from Eq. (1.15) by dropping the label KS and by replacing everywhere ρ^{out} by ρ^{in}, yielding [note cancellations between the third and fourth terms on the right-hand-side of Eq. (1.15)].

$$E_{\text{Harris}}[\rho^{\text{in}}] = E_I + \sum_{i=1}^{\text{occ}} \varepsilon_i^{\text{out}} - \int \left\{ \frac{1}{2} V_H[\rho^{\text{in}}(\mathbf{r})] + V_{xc}[\rho^{\text{in}}(\mathbf{r})] \right\} \rho^{\text{in}}(\mathbf{r}) d\mathbf{r} +$$
$$\int \mathcal{E}_{xc}[\rho^{\text{in}}(\mathbf{r})] d\mathbf{r}. \tag{1.16}$$

$\varepsilon_i^{\text{out}}$ are the single-particle solutions (non-self-consistent) of Eq. (1.11), with $V_{KS}[\rho^{\text{in}}(\mathbf{r})$ [see Eq. (1.12)].

As stated above this result is accurate to second order in $\rho^{\text{in}} - \rho_{KS}$ (alternatively in $\rho^{\text{in}} - \rho^{\text{out}}$), thus approximating the self-consistent total energy $E_{KS}[\rho_{KS}]$.

Obviously the accuracy of the results obtained via Eq. (1.16) depend on the choice of the input density ρ^{in}. In electronic structure calculations where the corpuscular nature of the ions is included (i.e., all-electron or pseudo-potential calculations), a natural choice for ρ^{in} consists of a superposition of atomic site densities, as suggested originally by Harris. In the case of jellium calculations, we have shown [3] that an accurate approximation to the KS-DFT total energy is obtained by using the Harris functional with the input density, ρ^{in}, in Eq. (1.16) evaluated from an Extended-Thomas-Fermi (ETF)-DFT calculation.

The ETF-DFT energy functional, $E_{ETF}[\rho]$, is obtained by replacing the kinetic energy term in Eq. (1.9) by a kinetic energy density-functional in the spirit of the Thomas-Fermi approach [67], but comprising terms up to fourth-order in the density gradients [48, 68]. The optimal ETF-DFT total energy is then obtained by minimization of $E_{ETF}[\rho]$ with respect to the density. In our calculations, we use for the trial densities parametrized profiles $\rho(\mathbf{r}; \{\gamma_i\})$ with $\{\gamma_i\}$ as variational parameters (the ETF-DFT optimal density is denoted as ρ_{ETF}). The single-particle eigenvalues, $\{\varepsilon_i^{\text{out}}\}$, in Eq. (1.16) are obtained then as the solutions to a single-particle Hamiltonian,

$$\widehat{H}_{ETF} = -\frac{\hbar^2}{2m} \nabla^2 + V_{ETF}, \tag{1.17}$$

where V_{ETF} is given by Eq. (1.12) with $\rho_{KS}(\mathbf{r})$ replaced by $\rho_{ETF}(\mathbf{r})$. These single-particle eigenvalues will be denoted by $\{\widetilde{\varepsilon}_i\}$

As is well known, the ETF-DFT does not contain shell effects [48–50]. Consequently, the corresponding density ρ_{ETF} can be taken à la Strutinsky as the smooth part, $\widetilde{\rho}$, of the KS density, ρ_{KS}. Accordingly, E_{ETF} is identified with the smooth

part $\widetilde{E}$ in Eq. (1.1) (in the following, the "ETF" subscript and " $\widetilde{\;}$ " can be used interchangeably). Since, as aforementioned, $E_{\text{Harris}}[\rho_{ETF}]$ approximates well [i.e., to second order in $(\rho_{ETF} - \rho_{KS})$] the self-consistent total energy $E_{KS}[\rho_{KS}]$, it follows from Eq. (1.1), with $E_{\text{Harris}}[\rho_{ETF}]$ taken as the expression for E_{total}, that the shell-correction, ΔE_{sh}, is given by

$$\Delta E_{sh} = E_{\text{Harris}}[\rho_{ETF}] - E_{ETF}[\rho_{ETF}] \equiv E_{sh}[\widetilde{\rho}] - \widetilde{E}[\widetilde{\rho}]. \tag{1.18}$$

Defining,

$$T_{sh} = \sum_{i=1}^{\text{occ}} \widetilde{\varepsilon}_i - \int \rho_{ETF}(\mathbf{r}) V_{ETF}(\mathbf{r}) d\mathbf{r}, \tag{1.19}$$

and denoting the total energy E_{Harris} by E_{sh}, i.e., by identifying

$$E_{sh} \equiv E_{\text{Harris}}, \tag{1.20}$$

we obtain

$$E_{sh}[\widetilde{\rho}] = \{T_{sh} - \widetilde{T}[\widetilde{\rho}]\} + \widetilde{E}[\widetilde{\rho}], \tag{1.21}$$

where $\widetilde{T}[\widetilde{\rho}]$ is the ETF kinetic energy, given to fourth-order gradients by the expression [68],

$$T_{ETF}[\rho] = \frac{\hbar^2}{2m} \int \left\{ \frac{3}{5}(3\pi^2)^{2/3}\rho^{5/3} + \frac{1}{36}\frac{(\nabla\rho)^2}{\rho} + \frac{1}{270}(3\pi^2)^{-2/3}\rho^{1/3} \right.$$
$$\left. \times \left[\frac{1}{3}\left(\frac{\nabla\rho}{\rho}\right)^4 - \frac{9}{8}\left(\frac{\nabla\rho}{\rho}\right)^2\frac{\Delta\rho}{\rho} + \left(\frac{\Delta\rho}{\rho}\right)^2 \right] \right\} d\mathbf{r}, \tag{1.22}$$

which as noted before does not contain shell effects. Therefore, the shell correction term in Eq. (1.1) [or Eq. (1.18)] is given by a difference between kinetic energy terms,

$$\Delta E_{sh} = T_{sh} - \widetilde{T}[\widetilde{\rho}]. \tag{1.23}$$

One should note that the above derivation of the shell correction does not involve a Strutinsky averaging procedure of the kinetic energy operator. Rather it is based on using ETF quantities as the smooth part for the density, $\widetilde{\rho}$, and energy, $\widetilde{E}$. Other descriptions of the smooth part may result in different shell-correction terms.

To check the accuracy of this procedure, we have compared results of calculations using the functional E_{sh} [Eq. (1.21)] with available Kohn-Sham calculations. In general, the optimized density from the minimization of the ETF-DFT functional can be obtained numerically as a solution of the differential equation

$$\frac{\delta T_{ETF}[\rho]}{\delta\rho(\mathbf{r})} + V_{ETF}[\rho(\mathbf{r})] = \mu, \tag{1.24}$$

where μ is the chemical potential. As mentioned already, for the jellium DFT-SCM calculations, we often use a trial density profile in the ETF-DFT variation which is
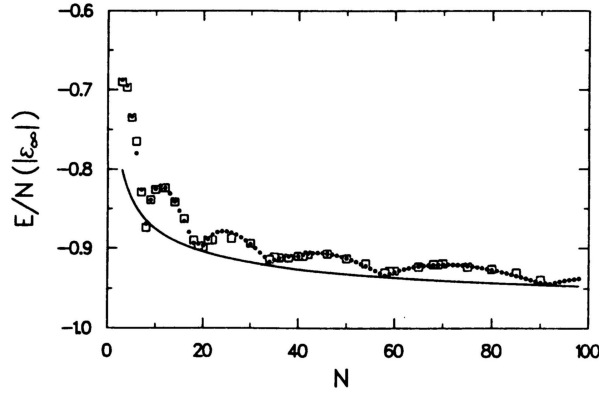
Fig. 1.2.   Total energy per atom of neutral sodium clusters (in units of the absolute value of the energy per atom in the bulk, $|\varepsilon_\infty| = 2.252\ eV$). Solid circles: DFT-SCM results (see text for details). The solid line is the ETF result (smooth contribution). In both cases, a spherical jellium background was used. Open squares: Kohn-Sham DFT results from Ref. [69]. The excellent agreement (a discrepancy of only 1%) between the DFT-SCM and the Kohn-Sham DFT approach is to be stressed.

chosen as,

$$\rho(r) = \frac{\rho_0}{\left[1 + \exp\left(\frac{r-r_0}{\alpha}\right)\right]^\gamma},\qquad(1.25)$$

with r_0, α, and γ as variational parameters that minimize the ETF-DFT functional (for other closely related parametrizations, cf. Refs. [49, 50]).

Figure 1.2 displays results of the present shell correction approach for the total energies of neutral sodium clusters. The results of the shell correction method for ionization potentials of sodium clusters are displayed in Fig. 1.3. The excellent agreement between the oscillating results obtained via our DFT-SCM theory and the Kohn-Sham results (cf., e.g., Ref. [69]) is evident. To further illustrate the two components (smooth contribution and shell correction) entering into our approach, we also display the smooth parts resulting from the ETF method. (In all calculations, the Gunnarsson-Lundqvist exchange and correlation energy functionals were used; see Refs. [3, 23].)

1.3. Applications of DFT-SCM

1.3.1. *Metal clusters*

1.3.1.1. *Charging of metal clusters*

Investigations of metal clusters based on DFT methods and self-consistent solutions of the Kohn-Sham equations (employing either a positive jellium background or maintaining the discrete ionic cores) have contributed significantly to our understanding of these systems [69–72]. However, even for singly negatively charged

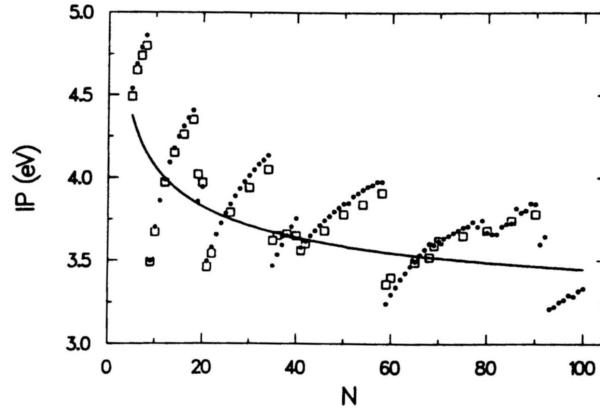12   *Constantine Yannouleas and Uzi Landman*

Fig. 1.3.   Ionization potentials for sodium clusters. Solid circles: IPs calculated with the DFT-SCM (see text for details). The solid line corresponds to the ETF results (smooth contribution). In both cases, a spherical jellium background was used. Open squares: Kohn-Sham DFT results from Ref. [69]. The excellent agreement (a discrepancy of only 1-2%) between the DFT shell correction method and the full Kohn-Sham approach should be noted.

metal clusters (M_N^-), difficulties may arise due to the failure of the solutions of the KS equations to converge, since the eigenvalue of the excess electron may iterate to a positive energy [73]. While such difficulties are alleviated for M_N^- clusters via self-interaction corrections (SIC) [74, 75], the treatment of multiply charged clusters $(M_N^{Z-},\ Z > 1)$ would face similar difficulties in the metastability region against electronic autodetachment through a Coulombic barrier. In the following we are applying our DFT-SCM approach, described in the previous section, to these systems [3, 23, 24] (for the jellium background, we assume spherical symmetry, unless otherwise stated; for a discussion of cluster deformations, see Sec. A.1).

1.3.1.2. *Electron affinities and borders of stability*

The smooth multiple electron affinities $\widetilde{A}_Z$ prior to shell corrections are defined as the difference in the total energies of the clusters

$$\widetilde{A}_Z = \widetilde{E}(vN, vN + Z - 1) - \widetilde{E}(vN, vN + Z), \qquad (1.26)$$

where N is the number of atoms, v is the valency and Z is the number of excess electrons in the cluster (e.g., first and second affinities correspond to $Z = 1$ and $Z = 2$, respectively). vN is the total charge of the positive background. Applying the shell correction in Eq. (1.23), we calculate the full electron affinity as

$$A_Z^{sh} - \widetilde{A}_Z = \Delta E_{sh}(vN, vN + Z - 1) - \Delta E_{sh}(vN, vN + Z). \qquad (1.27)$$

A positive value of the electron affinity indicates stability upon attachment of an extra electron. Figure 1.4 displays the smooth, as well as the shell corrected, first and second electron affinities for sodium clusters with $N < 100$. Note that
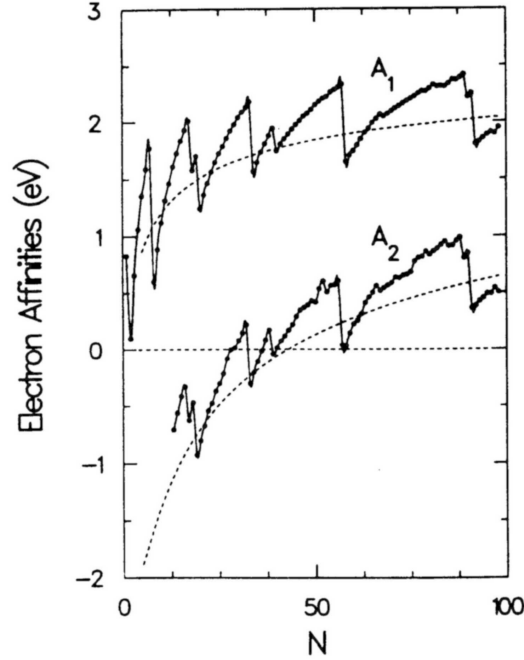
Fig. 1.4.   Calculated first (A_1) and second (A_2) electron affinities of sodium clusters as a function of the number of atoms N. Both their smooth part (dashed lines) and the shell-corrected affinities (solid circles) are shown. A spherical jellium background was used.

$\widetilde{A}_2$ becomes positive above a certain critical size, implying that the second electron in doubly negatively charged sodium clusters with $N < N_{\text{cr}}^{(2)} = 43$ might not be stably attached. The shell effects, however, create two islands of stability about the magic clusters Na_{32}^{2-} and Na_{38}^{2-} (see A_2^{sh} in Fig. 1.4). To predict the critical cluster size $N_{\text{cr}}^{(Z)}$, which allows stable attachment of Z excess electrons, we calculated the smooth electron affinities of sodium clusters up to $N = 255$ for $1 \leq Z \leq 4$, and display the results in Fig. 1.5. We observe that $N_{\text{cr}}^{(3)} = 205$, while $N_{\text{cr}}^{(4)} > 255$.

The similarity of the shapes of the curves in Fig. 1.5, and the regularity of distances between them, suggest that the smooth electron affinities can be fitted by a general expression of the form:

$$\widetilde{A}_Z = \widetilde{A}_1 - \frac{(Z-1)e^2}{R+\delta} = W - \beta \frac{e^2}{R+\delta} - \frac{(Z-1)e^2}{R+\delta}, \qquad (1.28)$$

where the radius of the positive background is $R = r_s N^{1/3}$. From our fit, we find that the constant W corresponds to the bulk work function. In all cases, we find $\beta = 5/8$, which suggests a close analogy with the classical model of the image charge [76, 77]. For the spill-out parameter, we find a weak size dependence as $\delta = \delta_0 + \delta_2/R^2$. The contribution of δ_2/R^2, which depends on Z, is of importance only for smaller sizes and does not affect substantially the critical sizes (where the curve

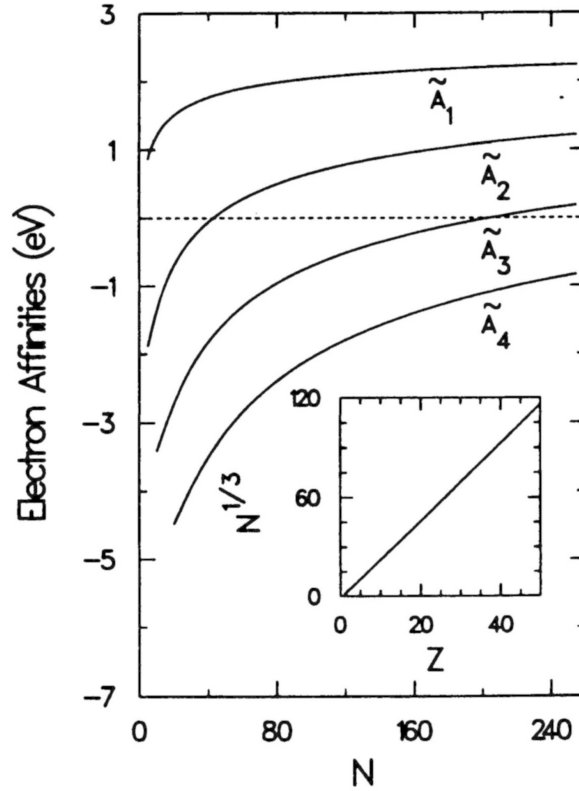14   *Constantine Yannouleas and Uzi Landman*

Fig. 1.5.   Calculated smooth electron affinities $\widetilde{A}_Z$, $Z = 1\text{-}4$, for sodium clusters as a function of the number of atoms N (Z is the number of excess electrons). A spherical jellium background was used. Inset: The electron *drip* line for sodium clusters. Clusters stable against spontaneous electron emission are located above this line. While for spherical symmetry, as seen from Fig. 1.4, shell effects influence the border of stability, shell-corrected calculations [25] including deformations (see the appendix) yield values close to the drip line (shown in the inset) which was obtained from the smooth contributions.

crosses the zero line), and consequently δ_2 can be neglected in such estimations. Using the values obtained by us for $\widetilde{A}_1$ of sodium clusters (namely, $W = 2.9\ eV$ which is also the value obtained by KS-DFT calculations for an infinite planar surface [78], $\delta_0 = 1.16\ a.u.$; with $R = r_s N^{1/3}$, and $r_s = 4.00\ a.u.$), we find for the critical sizes when the l.h.s. of Eq. (1.28) is set equal to zero, $N_{\text{cr}}^{(2)} = 44$, $N_{\text{cr}}^{(3)}) = 202$, $N_{\text{cr}}^{(4)} = 554$, and $N_{\text{cr}}^{(5)} = 1177$, in very good agreement with the values obtained directly from Fig. 1.5.

The curve that specifies $N_{\text{cr}}^{(Z)}$ in the (Z, N) plane defines the border of stability for spontaneous electron decay. In nuclei, such borders of stability against spontaneous proton or neutron emission are known as nucleon drip lines [79]. For the case of sodium clusters, the electron drip line is displayed in the inset of Fig. 1.5.
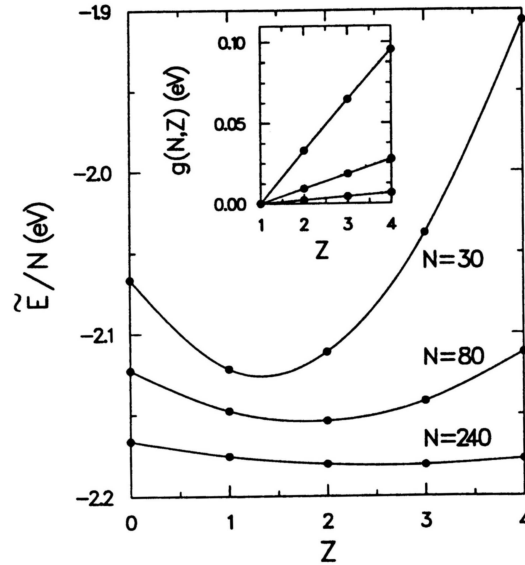
Fig. 1.6.   Calculated smooth total energy per atom as a function of the excess negative charge Z for the three families of sodium clusters with $N = 30$, $N = 80$, and $N = 240$ atoms. A spherical jellium background was used. As the straight lines in the inset demonstrate, the curves are parabolic. We find that they can be fitted by Eq. (1.29). See text for an explanation of how the function $g(N, Z)$ was extracted from the calculations.

1.3.1.3. *Critical sizes for potassium and aluminum*

While in this investigation we have used sodium clusters as a test system, the methodology and conclusions extend to other materials as well. Thus given a calculated or measured bulk work function W, and a spill-out parameter (δ_0 typically of the order of 1-2 *a.u.*, and neglecting δ_2), one can use Eq. (1.28), with $\widetilde{A}_Z = 0$, to predict critical sizes for other materials. For example, our calculations for potassium ($r_s = 4.86$ *a.u.*) give fitted values $W = 2.6$ *eV* (compared to a KS-DFT value of 2.54 *eV* for a semi-infinite planar surface with $r_s = 5.0$ *a.u.* [78]) and $\delta_0 = 1.51$ *a.u.* for $\delta_2 = 0$, yielding $N_{\mathrm{cr}}^{(2)} = 33$, $N_{\mathrm{cr}}^{(3)} = 152$, and $N_{\mathrm{cr}}^{(4)} = 421$.

As a further example, we give our results for a trivalent metal, i.e. aluminum ($r_s = 2.07$ *a.u.*), for which our fitted values are $W = 3.65$ *eV* (compared to a KS-DFT value of 3.78 *eV* for a semi-infinite plane surface, with $r_s = 2.0$ *a.u.* [78]) and $\delta_0 = 1.86$ *a.u.* for $\delta_2 = 0$, yielding $N_{\mathrm{cr}}^{(2)} = 40$ (121 electrons), $N_{\mathrm{cr}}^{(3)} = 208$ (626 electrons), and $N_{\mathrm{cr}}^{(4)} = 599$ (1796 electrons).

1.3.1.4. *Metastability against electron autodetachment*

The multiply charged anions with negative affinities do not necessarily exhibit a positive total energy. To illustrate this point, we display in Fig. 1.6 the calculated total energies per atom ($\widetilde{E}(N, Z)/N$) as a function of excess charge (Z) for clus-

ters containing 30, 80, and 240 sodium atoms. These sizes allow for exothermic attachment of maximum one, two, or three excess electrons, respectively.

As was the case with the electron affinities, the total-energy curves in Fig. 1.6 show a remarkable regularity, suggesting a parabolic dependence on the excess charge. To test this conjecture, we have extracted from the calculated total energies the quantity $g(N, Z) = G(N, Z)/N$ where $G(N, Z) = [\widetilde{E}(N, Z) - \widetilde{E}(N, 0)]/Z + \widetilde{A}_1(N)$, and have plotted it in the inset of Fig. 1.6 as a function of the excess negative charge Z. The dependence is linear to a remarkable extent; for $Z = 1$ all three lines cross the energy axis at zero. Combined with the results on the electron affinities, this indicates that the total energies have the following dependence on the excess number of electrons (Z):

$$\widetilde{E}(Z) = \widetilde{E}(0) - \widetilde{A}_1 Z + \frac{Z(Z-1)e^2}{2(R+\delta)}, \tag{1.29}$$

where the dependence on the number of atoms in the cluster is not explicitly indicated.

This result is remarkable in its analogy with the classical image-charge result of van Staveren *et al.* [77]. Indeed, the only difference amounts to the spill-out parameter δ_0 and to the weak dependence on Z through δ_2. This additional Z-dependence becomes negligible already for the case of 30 sodium atoms.

For metastable multiply-charged cluster anions, electron emission (autodetachment) will occur via tunneling through a barrier (shown in Fig. 1.7). However, to reliably estimate the electron emission, it is necessary to correct the LDA effective potential for self-interaction effects. We performed a self-interaction correction of the Amaldi type [73] for the Hartree term and extended it to the exchange-correlation contribution to the total energy as follows: $E_{\text{xc}}^{\text{SIC}}[\rho] = E_{\text{xc}}^{\text{LDA}}[\rho] - N_e E_{\text{xc}}^{\text{LDA}}[\rho/N_e]$, where $N_e = vN + Z$ is the total number of electrons. This self-interaction correction is akin to the orbitally-averaged-potential method [73]. Minimizing the SIC energy functional for the parameters r_0, α, and γ, we obtained the effective SIC potential for Na_{18}^{2-} shown in Fig. 1.7, which exhibits the physically correct asymptotic behavior [80].

The spontaneous electron emission through the Coulombic barrier is analogous to that occurring in proton radioactivity from neutron-deficient nuclei [81], as well as in alpha-particle decay. The transition rate is $\lambda = \ln 2/T_{1/2} = \nu P$, where ν is the attempt frequency and P is the transmission coefficient calculated in the WKB method (for details, cf. Ref. [81]). For the $2s$ electron in Na_{18}^{2-} (cf. Fig. 1.7), we find $\nu = 0.73 \; 10^{15} \; Hz$ and $P = 4.36 \; 10^{-6}$, yielding $T_{1/2} = 2.18 \; 10^{-10} \; s$. For a cluster size closer to the drip line (see Fig. 1.5), e.g. Na_{35}^{2-}, we find $T_{1/2} = 1.13 \; s$.

Finally, the exression in Eq. (1.29) for the total energy can be naturally extended to the case of multiply *positively* charged metal clusters by setting $Z = -z$, with $z > 0$. The ensuing equation retains the same dependence on the excess positive charge z, but with the negative value of the first affinity, $-\widetilde{A}_1$, replaced by the positive value of the first ionization potential, $\widetilde{I}_1 = W + (3/8)e^2/(R+\delta)$, a result
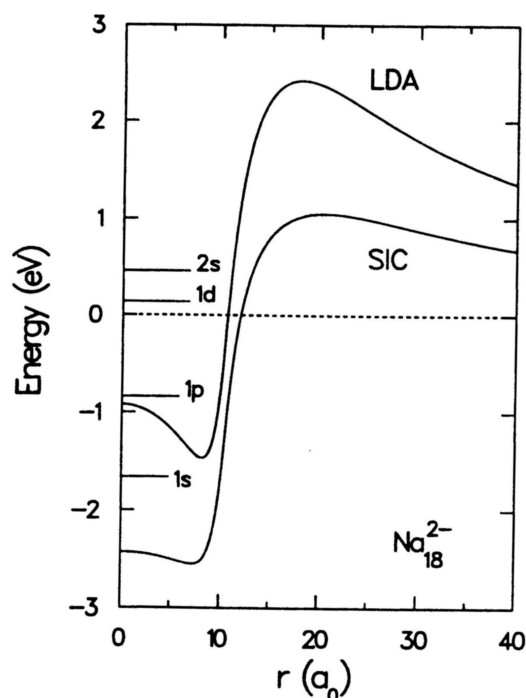
Fig. 1.7.   The DFT (LDA) and the corresponding self-interaction corrected potential for the metastable Na_{18}^{2-} cluster. A spherical jellium background was used. The single-particle levels of the SIC potential are also shown. Unlike the LDA, this latter potential exhibits the correct asymptotic behavior. The $2s$ and $1d$ electrons can be emitted spontaneously by tunneling through the Coulombic barrier of the SIC potential. Distances in units of the Bohr radius, a_0. The specified single-particle levels are associated with the SIC potential.

that has been suggested from earlier measurements on multiply charged potassium cations [82]. Naturally, the spill-out parameter δ assumes different values than in the case of the anionic clusters.

1.3.2. *Neutral and multiply charged fullerenes*

1.3.2.1. *Stabilized jellium approximation - The generalized DFT-SCM*

Fullerenes and related carbon structures have been extensively investigated using *ab initio* density-functional-theory methods and self-consistent solutions of the Kohn-Sham (KS) equations [83, 84]. For metal clusters, replacing the ionic cores with a uniform jellium background was found to describe well their properties within the KS-DFT method [58]. Motivated by these results, several attempts to apply the jellium model in conjunction with DFT to investigations of fullerenes have appeared recently [39, 85–87]. Our approach [39] differs from the earlier ones in several aspects and, in particular, in the adaptation to the case of finite systems of the stabilized-

jellium (or structureless pseudopotential) energy density functional (see Eq. (1.30) below and Ref. [73]).

An important shortcoming of the standard jellium approximation for fullerenes (and other systems with high density, i.e., small r_s) results from a well-known property of the jellium at high electronic densities, namely that the jellium is unstable and yields negative surface-energy contribution to the total energy [73], as well as unreliable values for the total energy. These inadequacies of the standard jellium model can be rectified by pseudopotential corrections. A modified-jellium approach which incorporates such pseudopotential corrections and is particularly suited for our purposes here, is the *structureless pseudopotential* model or *stabilized jellium* approximation developed in Ref. [73].

In the stabilized jellium, the total energy E_{pseudo}, as a functional of the electron density $\rho(\mathbf{r})$, is given by the expression

$$E_{pseudo}[\rho, \rho_+] = E_{jell}[\rho, \rho_+] + \langle \delta v \rangle_{WS} \int \rho(\mathbf{r})\mathcal{U}(\mathbf{r})d\mathbf{r} - \widetilde{\varepsilon} \int \rho_+(\mathbf{r})d\mathbf{r}, \qquad (1.30)$$

where by definition the function $\mathcal{U}(\mathbf{r})$ equals unity inside, but vanishes, outside the jellium volume. ρ_+ is the density of the positive jellium background (which for the case of C_{60} is taken as a spherical shell, of a certain width $2d$, centered at 6.7 *a.u.*). E_{pseudo} in Eq. (1.30) is the standard jellium-model total energy, E_{jell}, modified by two corrections. The first correction adds the effect of an average (i.e., averaged over the volume of a Wigner-Seitz cell) difference potential, $\langle \delta v \rangle_{WS}\mathcal{U}(\mathbf{r})$, which acts on the electrons in addition to the standard jellium attraction and is due to the atomic pseudopotentials (in this work, we use the Ashcroft empty-core pseudopotential, specified by a core radius r_c, as in Ref. [73]). The second correction subtracts from the jellium energy functional the spurious electrostatic self-repulsion of the positive background within each cell; this term makes no contribution to the effective electronic potential.

Following Ref. [73], the bulk stability condition (Eq. (25) in Ref. [73]) determines the value of the pseudopotential core radius r_c, as a function of the bulk Wigner-Seitz radius r_s. Consequently, the difference potential can be expressed solely as a function of r_s as follows (energies in *Ry*, distances in *a.u.*):

$$\langle \delta v \rangle_{WS} = -\frac{2}{5}\left(\frac{9\pi}{4}\right)^{2/3}r_s^{-2} + \frac{1}{2\pi}\left(\frac{9\pi}{4}\right)^{1/3}r_s^{-1} + \frac{1}{3}r_s\frac{d\varepsilon_c}{dr_s}, \qquad (1.31)$$

where ε_c is the per particle electron-gas correlation energy (in our calculation, we use the Gunnarsson-Lundqvist exchange and correlation energy functionals; see Refs. [3, 23]).

The electrostatic self-energy, $\widetilde{\varepsilon}$, per unit charge of the uniform positive jellium is given by

$$\widetilde{\varepsilon} = 6\upsilon^{2/3}/5r_s, \qquad (1.32)$$

where υ is the valence of the atoms ($\upsilon = 4$ for carbon).

1.3.2.2. *ETF electron-density profile*

To apply the ETF-DFT method to carbon fullerenes, we generalize it by employing potential terms according to the stabilized-jellium functional in Eq. (1.30).

Another required generalization consists in employing a parametrized electron-density profile that accounts for the hollow cage-structure of the fullerenes. Such a density profile is provided by the following adaptation of a generalization of an inverse Thomas-Fermi distribution, used earlier in the context of nuclear physics [88], i.e.,

$$\rho(r) = \rho_0 \left(\frac{F_{i,o} \sinh[w_{i,o}/\alpha_{i,o}]}{\cosh[w_{i,o}/\alpha_{i,o}] + \cosh[(r - R)/\alpha_{i,o}]} \right)^{\gamma_{i,o}}, \qquad (1.33)$$

where $R = 6.7$ *a.u.* is the radius of the fullerene cage. w, α, and γ are variables to be determined by the ETF-DFT minimization. For $R = 0$ and large values of w/α, expression (1.33) approaches the more familiar inverse Thomas-Fermi distribution, with w the width, α the diffuseness and γ the asymmetry of the profile around $r = w$. There are a total of six parameters to be determined, since the indices (i, o) stand for the regions inside ($r < R$) and outside ($r > R$) the fullerene cage. $F_{i,o} = (\cosh[w_{i,o}/\alpha_{i,o}] + 1)/\sinh[w_{i,o}/\alpha_{i,o}]$ is a constant guaranteeing that the two parts of the curve join smoothly at $r = R$. The density profile in Eq. (1.33) peaks at $r = R$ and then falls towards smaller values both inside and outside the cage (see top panel of Fig. 1.8).

1.3.2.3. *Shell correction and icosahedral splitting*

To apply the SCM to the present case, the potential V_{ETF} in Eq. (1.19) is replaced by the stabilized-jellium LDA potential shown in Fig. 1.8. After some rearrangements, the shell-corrected total energy $E_{sh}[\widetilde{\rho}]$ in the stabilized-jellium case can be written in functional form as follows [compare to Eq. (1.21), see also Eq. (1.16)].

$$E_{sh}[\widetilde{\rho}] = \sum_i \widetilde{\varepsilon}_i - \int \left\{ \frac{1}{2} \widetilde{V}_H(\mathbf{r}) + \widetilde{V}_{xc}(\mathbf{r}) \right\} \widetilde{\rho}(\mathbf{r}) d\mathbf{r}$$
$$+ \int \widetilde{\mathcal{E}}_{xc}[\widetilde{\rho}(\mathbf{r})] d\mathbf{r} + E_I - \widetilde{\varepsilon} \int \rho_+(\mathbf{r}) d\mathbf{r}, \qquad (1.34)$$

Heretofore, the point-group icosahedral symmetry of C_{60} was not considered, since the molecule was treated as a spherically symmetric cage. This is a reasonable zeroth-order approximation as noticed by several authors [83, 87, 89, 90]. However, considerable improvement is achieved when the effects of the point-group icosahedral symmetry are considered as a next-order correction (mainly the lifting of the angular momentum degeneracies).

The method of introducing the icosahedral splittings is that of the crystal field theory [91]. Thus, we will use the fact that the bare electrostatic potential from the ionic cores, considered as point charges, acting upon an electron, obeys the
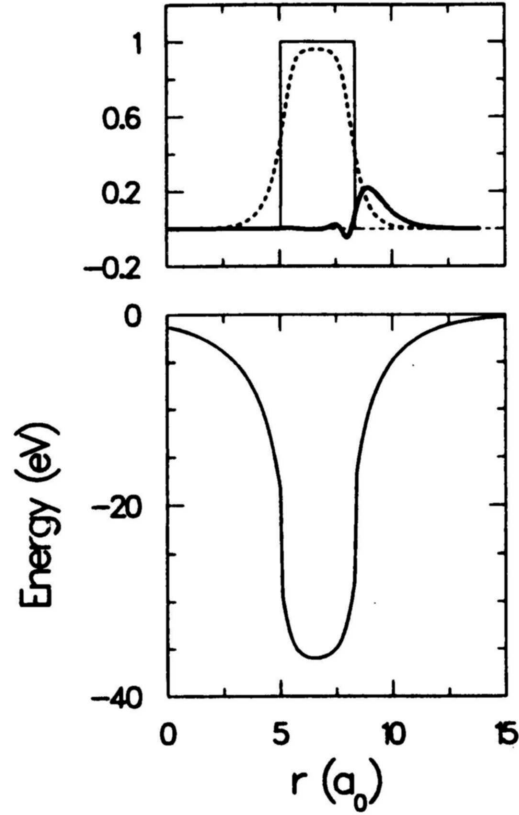
20   *Constantine Yannouleas and Uzi Landman*

Fig. 1.8.   Bottom panel: The stabilized-jellium LDA potential obtained by the ETF method
for the neutral C_{60} molecule. The Wigner-Seitz radius for the jellium bacground is 1.23 $a.u.$
Note the asymmetry of the potential about the minimum. The associated difference potential
$\langle \delta v \rangle_{WS} = -9.61 \ eV$.
Top panel: Solid line: Radial density of the positive jellium background. Dashed line: ETF
electronic density. Note its asymmetry about the maximum. Thick solid line: The difference
(multiplied by 10) of electronic ETF densities between C_{60}^{5-} and C_{60}. It illustrates that the
excess charge accumulates in the outer perimeter of the total electronic density. All densities are
normalized to the density of the positive jellium background.

well-known expansion theorem [91]

$$U(\mathbf{r}) = -v e^2 \sum_i \frac{1}{|\mathbf{r} - \mathbf{r}_i|} = -\sum_{l=0}^{\infty} \sum_{m=-l}^{l} \kappa_l(r) C_l^m Y_l^m(\theta, \phi), \qquad (1.35)$$

where the angular coefficients C_l^m are given through the angular coordinates θ_i, ϕ_i
of the carbon atomic cores, namely,

$$C_l^m = \sum_i Y_l^{m*}(\theta_i, \phi_i), \qquad (1.36)$$

where $*$ denotes complex conjugation.

Shell-correction and orbital-free density-functional methods for finite systems   21
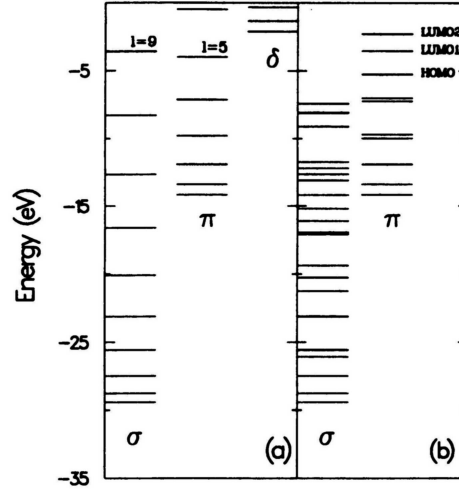

Fig. 1.9.   (a) The single-particle levels of the ETF-LDA potential for C_{60} shown in Fig. 1.8. Because of the spherical symmetry, they are characterized by the two principle quantum numbers n_r and l, where n_r is the number of radial nodes and l the angular momentum. They are grouped in three bands labeled σ ($n_r = 0$), π ($n_r = 1$), and δ ($n_r = 2$). Each band starts with an $l = 0$ level.
(b) The single-particle levels for C_{60} after the icosahedral splittings are added to the spectra of (a). The tenfold degenerate HOMO (h_u) and the sixfold degenerate LUMO1 (t_{1u}) and LUMO2 (t_{1g}) are denoted; they originate from the spherical $l = 5$ and $l = 6$ (t_{1g}) π levels displayed in panel (a). For the σ electrons, the icosahedral perturbation strongly splits the $l = 9$ level of panel (a). There result five sublevels which straddle the σ-electron gap as follows: two of them (the eightfold degenerate g_u, and the tenfold degenerate h_u) move down and are fully occupied resulting in a shell closure (180 σ electrons in total). The remaining unoccupied levels, originating from the $l = 9$ σ level, are sharply shifted upwards and acquire positive values.

We take the radial parameters $\kappa_l(r)$ as constants, and determine their value by adjusting the icosahedral single-particle spectra ε_i^{ico} to reproduce the pseudopotential calculation of Ref. [83], which are in good agreement with experimental data. Our spectra without and with icosahedral splitting are shown in Fig. 1.9(a) and Fig. 1.9(b), respectively.

We find that a close reproduction of the results of *ab initio* DFT calculations [83, 92, 93] is achieved when the Wigner-Seitz radius for the jellium background is 1.23 *a.u.* The shell corrections, ΔE_{sh}^{ico}, including the icosahedral splittings are calculated using the icosahedral single-particle energies ε_i^{ico} in Eq. (1.19). The average quantities ($\widetilde{\rho}$ and $\widetilde{V}$) are maintained as those specified through the ETF variation with the spherically symmetric profile of Eq. (1.33). This is because the first-order correction to the total energy (resulting from the icosahedral perturbation) vanishes, since the integral over the sphere of a spherical harmonic Y_l^m ($l > 0$) vanishes.

                              Constantine Yannouleas and Uzi Landman

1.3.2.4. *Ionization potentials and electron affinities*

Having specified the appropriate Wigner-Seitz radius r_s and the parameters κ_l of
the icosahedral crystal field through a comparison with the pseudopotential DFT
calculations for the neutral C_{60}, we calculate the total energies of the cationic and
anionic species by allowing for a change in the total electronic charge, namely by
imposing the constraint

$$4\pi \int \rho(r)r^2 dr = 240 \pm x, \qquad (1.37)$$

where $\rho(r)$ is given by Eq. (1.33). The shell-corrected and icosahedrally perturbed
first and higher ionization potentials I_x^{ico} are defined as the difference of the ground-
state shell-corrected total energies E_{sh}^{ico} as follows:

$$I_x^{ico} = E_{sh}^{ico}(N_e = 240 - x; Z = 240) - E_{sh}^{ico}(N_e = 240 - x + 1; Z = 240), \quad (1.38)$$

where N_e is the number of electrons in the system and x is the number of excess
charges on the fullerenes (for the excess charge, we will find convenient to use two
different notations x and z related as $x = |z|$. A negative value of z corresponds to
positive excess charges). $Z = 240$ denotes the total positive charge of the jellium
background.

   The shell-corrected and icosahedrally perturbed first and higher electron affini-
ties A_x^{ico} are similarly defined as

$$A_x^{ico} = E_{sh}^{ico}(N_e = 240 + x - 1; Z = 240) - E_{sh}^{ico}(N_e = 240 + x; Z = 240). \quad (1.39)$$

   We have also calculated the corresponding average quantities $\widetilde{I}_x$ and $\widetilde{A}_x$, which
result from the ETF variation with spherical symmetry (that is without shell and
icosahedral symmetry corrections). Their definition is the same as in Eq. (1.38) and
Eq. (1.39), but with the index sh replaced by a tilde and the removal of the index
ico.

   In our calculations of the charged fullerene molecule, the r_s value and the icosa-
hedral splitting parameters (κ_l, see Eq. (1.35), and discussion below it) were taken
as those which were determined by our calculations of the neutral molecule, dis-
cussed in the previous section. The parameters which specify the ETF electronic
density (Eq. (1.33)) are optimized for the charged molecule, thus allowing for re-
laxation effects due to the excess charge. This procedure is motivated by results
of previous electronic structure calculations for C_{60}^+ and C_{60}^- [92, 93], which showed
that the icosahedral spectrum of the neutral C_{60} shifts almost rigidly upon charging
of the molecule.

   Shell-corrected and ETF calculated values of ionization potentials and electron
affinities, for values of the excess charge up to 12 units, are summarized in Table 1.1
(for $r_s = 1.23\ a.u.$)

Table 1.1.   ETF (spherically averaged, denoted by a tilde) and shell-corrected (denoted by a superscript *ico* to indicate that the icosahedral splittings of energy levels have been included) IPs and EAs of fullerenes $C_{60}^{x\pm}$. Energies in eV. $r_s = 1.23$ *a.u.*

x	$\widetilde{I}_x$	I_x^{ico}	$\widetilde{A}_x$	A_x^{ico}
1	5.00	7.40	2.05	2.75
2	7.98	10.31	−0.86	−0.09
3	10.99	13.28	−3.75	−2.92
4	14.03	16.25	−6.60	−5.70
5	17.09	19.22	−9.41	−8.41
6	20.18	22.20	−12.19	−11.06
7	23.29	25.24	−14.94	−14.85
8	26.42	28.31	−17.64	−17.24
9	29.57	31.30	−20.31	−19.49
10	32.73	34.39	−22.94	−21.39
11	35.92	39.36	−25.53	−22.93
12	39.12	42.51	−28.07	−23.85

1.3.2.5. *Charging energies and capacitance of fullerenes*

Figure 1.10(a) shows that the variation of the total ETF-DFT energy difference (appearance energies) $\Delta\widetilde{E}(z) = \widetilde{E}(z) - \widetilde{E}(0)$, as a function of excess charge z ($|z| = x$), exhibits a parabolic behavior. The inset in Fig. 1.10(a) exhibiting the quantity

$$\widetilde{g}(z) = \frac{\widetilde{E}(z) - \widetilde{E}(0)}{z} + \widetilde{A}_1, \qquad (1.40)$$

plotted versus z (open squares), shows a straight line which crosses the zero energy line at $z = 1$. As a result the total ETF-DFT energy has the form,

$$\widetilde{E}(z) = \widetilde{E}(0) + \frac{z(z-1)e^2}{2C} - \widetilde{A}_1 z. \qquad (1.41)$$

Equation (1.41) indicates that fullerenes behave on the average like a capacitor having a capacitance C (the second term on the rhs of Eq. (1.41) corresponds to the charging energy of a classical capacitor, corrected for the self-interaction of the excess charge [3, 23]). We remark that regarding the system as a classical conductor, where the excess charge accumulates on the outer surface, yields a value of $C = 8.32$ *a.u.* (that is the outer radius of the jellium shell). Naturally, the ETF calculated value for C is somewhat larger because of the quantal spill-out of the electronic charge density. Indeed, from the slope of $\widetilde{g}(z)$ we determine [94] $C = 8.84$ *a.u.*

A similar plot of the shell-corrected and icosahedrally modified energy differences $\Delta E_{sh}^{ico}(z) = E_{sh}^{ico}(z) - E_{sh}^{ico}(0)$ is shown in Fig. 1.10(b) (in the range $-2 \leq z \leq 4$, filled circles). The function $g_{sh}^{ico}(z)$, defined as in Eq. (1.40) but with the shell-corrected quantities ($\Delta E_{sh}^{ico}(z)$ and A_1^{ico}), is included in the inset to Fig. 1.10(a) (filled circles).
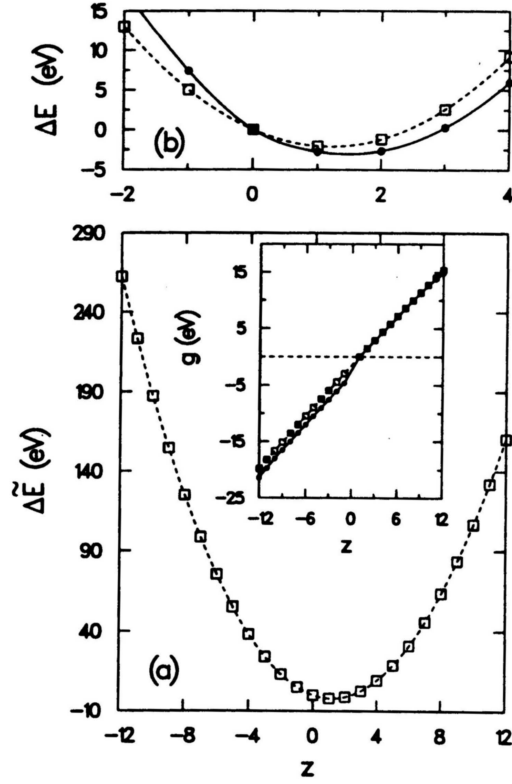
24   *Constantine Yannouleas and Uzi Landman*

Fig. 1.10.   (a) ETF-DFT total energy differences (appearance energies) $\Delta \widetilde{E}(z) = \widetilde{E}(z) - \widetilde{E}(0)$ as a function of the excess charge z ($z < 0$ corresponds to positive excess charge). Inset: The ETF function $\widetilde{g}(z)$ (open squares), and the shell-corrected function $g_{sh}^{ico}(z)$ (filled circles). For $z \geq 1$ the two functions are almost identical.
(b) magnification of the appearance-energy curves for the region $-2 \leq z \leq 4$. Filled circles: shell-corrected icosahedral values [$\Delta E_{sh}^{ico}(z) = E_{sh}^{ico}(z) - E_{sh}^{ico}(0)$]. Open squares: ETF-DFT values [$\Delta \widetilde{E}(z) = \widetilde{E}(z) - \widetilde{E}(0)$].

The shift discernible between $g_{sh}^{ico}(-1)$ and $g_{sh}^{ico}(1)$ is approximately 1.7 eV, and originates from the difference of shell effects on the IPs and EAs (see Table 1.1). The segments of the curve $g_{sh}^{ico}(z)$ in the inset of Fig. 1.10(a), corresponding to positively ($z < 0$) and negatively ($z > 0$) charged states, are again well approximated by straight lines, whose slope is close to that found for $\widetilde{g}(z)$. Consequently, we may approximate the charging energy, including shell-effects, as follows,

$$E_{sh}^{ico}(x) = E_{sh}^{ico}(0) + \frac{x(x-1)e^2}{2C} - A_1^{ico}x, \qquad (1.42)$$

for *negatively* charged states, and

$$E_{sh}^{ico}(x) = E_{sh}^{ico}(0) + \frac{x(x-1)e^2}{2C} + I_1^{ico}x, \qquad (1.43)$$

for *positively* charged states. Note that without shell-corrections (i.e., ETF only) $\widetilde{I}_1 - \widetilde{A}_1 = e^2/C = 27.2/8.84 \; eV \approx 3.1 \; eV$, because of the symmetry of Eq. (1.41) with respect to z, while the shell-corrected quantities are related as $I_1^{ico} - A_1^{ico} \approx e^2/C + \Delta_{sh}$, where the shell correction is $\Delta_{sh} \approx 1.55 \; eV$ (from Table 1.1, $I_1^{ico} - A_1^{ico} \approx 4.65 \; eV$).

Expression (1.42) for the negatively charged states can be rearranged as follows (energies in units of eV),

$$E_{sh}^{ico}(x) - E_{sh}^{ico}(0) = -2.99 + 1.54(x - 1.39)^2, \qquad (1.44)$$

in close agreement with the all-electron LDA result of Ref. [95].

Equations (1.42) and (1.43) can be used to provide simple analytical approximations for the higher IPs and EAs. Explicitly written, $A_x^{ico} \equiv E_{sh}^{ico}(x-1) - E_{sh}^{ico}(x) = A_1^{ico} - (x-1)e^2/C$ and $I_x^{ico} = I_1^{ico} + (x-1)e^2/C$. Such expressions have been used previously [96] with an assumed value for $C \approx 6.7 \; a.u.$ (i.e., the radius of the C_{60} molecule, as determined by the distance of carbon nuclei from the center of the molecule), which is appreciably smaller than the value obtained by us ($C = 8.84 \; a.u.$, see above) via a microscopic calculation. Consequently, using the above expression with our calculated value for $A_1^{ico} = 2.75 \; eV$ (see Table 1.1), we obtain an approximate value of $A_2^{ico} = -0.35 \; eV$ (compared to the microscopically calculated value of $-0.09 \; eV$ given in Table 1.1, and $-0.11 \; eV$ obtained by Ref. [95]) — indicating metastability of C_{60}^{2-} — while employing an experimental value for $A_1^{ico} = 2.74 \; eV$, a value of $A_2^{ico} = 0.68 \; eV$ was calculated in Ref. [96].

Concerning the cations, our expression (1.43) with a calculated $I_1^{ico} = 7.40 \; eV$ (see Table 1.1) and $C = 8.84 \; a.u.$ yields approximate values $18.5 \; eV$ and $31.5 \; eV$ for the appearance energies of C_{60}^{2+} and C_{60}^{3+} (compared to the microscopic calculated values of $17.71 \; eV$ and $30.99 \; eV$, respectively, extracted from Table 1.1, and $18.6 \; eV$ for the former obtained in Ref. [92]). Employing an experimental value for $I_1^{ico} = 7.54 \; eV$, corresponding values of $19.20 \; eV$ and $34.96 \; eV$ were calculated in Ref. [96]. As discussed in Ref. [97], these last values are rather high, and the origin of the discrepancy may be traced to the small value of the capacitance which was used in obtaining these estimates in Ref. [96].

A negative value of the second affinity indicates that C_{60}^{2-} is unstable against electron autodetachment. In this context, we note that the doubly negatively charged molecule C_{60}^{2-} has been observed in the gas phase and is believed to be a long-lived metastable species [98, 99]. Indeed, as we discuss in the next section, the small DFT values of A_2^{ico} found by us and by Ref. [95] yield lifetimes which are much longer than those estimated by a pseudopotential-like Hartree-Fock model calculation [98], where a value of $\sim 1 \; \mu s$ was estimated.

1.3.2.6. *Lifetimes of metastable anions, C_{60}^{x-}*

The second and higher electron affinities of C_{60} were found to be negative, which implies that the anions C_{60}^{x-} with $x \geq 2$ are not stable species, and can lower their

energy by emitting an electron. However, unless the number of excess electrons is large enough, the emission of an excess electron involves tunneling through a barrier. Consequently, the moderately charged anionic fullerenes can be described as metastable species possessing a decay lifetime.

To calculate the lifetime for electron autodetachmant, it is necessary to determine the proper potential that the emitted electron sees as it leaves the molecule. The process is analogous to alpha-particle radioactivity of atomic nuclei. The emitted electron will have a final kinetic energy equal to the negative of the corresponding higher EA. We estimate the lifetime of the decay process by using the WKB method, in the spirit of the theory of alpha-particle radioactivity, which has established that the main factor in estimating lifetimes is the relation of the kinetic energy of the emitted particle to the Coulombic tail, and not the details of the many-body problem in the immediate vicinity of the parent nucleus.

Essential in this approach is the determination of an appropriate single-particle potential that describes the transmission barrier. It is well known that the (DFT) LDA potential posseses the wrong tail, since it allows for the electron to spuriously interact with itself. A more appropriate potential would be one produced by the Self-Interaction Correction method of Ref. [78]. This potential has the correct Coulombic tail, but in the case of the fullerenes presents another drawback, namely Koopman's theorem is not satisfied to an extent adequate for calculating lifetimes [100]. In this context, we note that Koopman's theorem is known to be poorly satisfied for the case of fullerenes even in Hartree-Fock calculations [101]. Therefore, the HOMO corresponding to the emitted electron, calculated as described above, cannot be used in the WKB tunneling calculation.

Since the final energy of the ejected electron equals the negative of the value of the electron affinity, we seek a potential that, together with the icosahedral perturbation, yields a HOMO level in C_{60}^{x-} with energy $-A_x^{ico}$. We construct this potential through a self-interaction correction to the LDA potential as follows,

$$V_{WKB} = V_{LDA}[\widetilde{\rho}] - V_H[\frac{\widetilde{\rho}}{N_e}] - V_{xc}[\xi\frac{\widetilde{\rho}}{N_e}], \qquad (1.45)$$

where the parameter ξ is adjusted so that the HOMO level of C_{60}^{x-} equals $-A_x^{ico}$. In the above expression, the second term on the rhs is an average self-interaction Hartree correction which ensures a proper long-range behavior of the potential (i.e., correct Coulomb tail), and the third term is a correction to the short-range exchange-correlation.

For the cases of C_{60}^{2-} and C_{60}^{3-} such potentials are plotted in Fig. 1.11. We observe that they have the correct Coulombic tail, namely a tail corresponding to one electron for C_{60}^{2-} and to two electrons for C_{60}^{3-}. The actual barrier, however, through which the electron tunnels is the sum of the Coulombic barrier plus the contribution of the centrifugal barrier. As seen from Fig. 1.11, the latter is significant, since the HOMO in the fullerenes possesses a rather high angular momentum ($l = 5$), while being confined in a small volume.
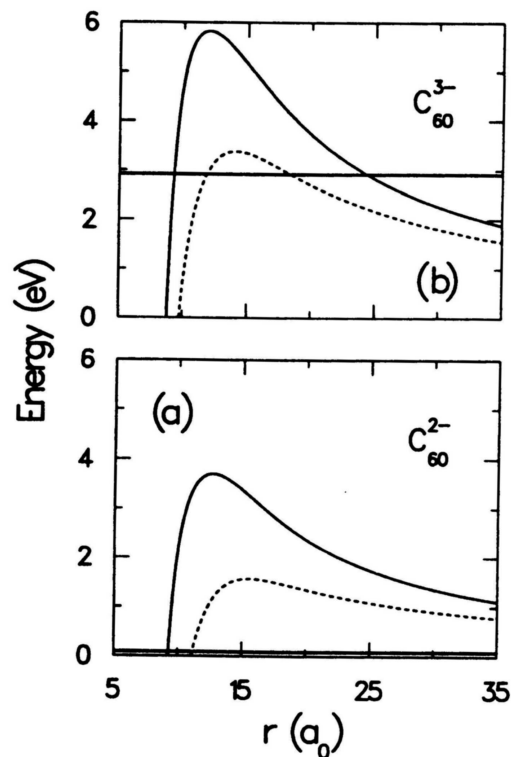
Shell-correction and orbital-free density-functional methods for finite systems   27

Fig. 1.11.   WKB effective barriers used to estimate lifetimes for C_{60}^{2-} (a) and C_{60}^{3-} (b). Dashed lines correspond to barriers due solely to Coulombic repulsion and solid lines to total barriers after adding the centrifugal components. The thick horizontal solid lines correspond to the negative of the associated electron affinities A_2^{ico} (a) and A_3^{ico} (b). In the case of C_{60}^{2-} [panel (a)], the horizontal solid line at $-A_2^{ico} = 0.09\ eV$ crosses the total barrier at an inside point $R_1 = 9.3\ a.u.$ and again at a distance very far from the center of the fullerene molecule, namely at an outer point $R_2 = -e^2/A_2^{ico} = 27.2/0.09\ a.u. = 302.2\ a.u.$ This large value of R_2, combined with the large centrifugal barrier, yields a macroscopic lifetime for the metastable C_{60}^{2-} (see text for details).

Using the WKB approximation [102], we estimate for C_{60}^{2-} a macroscopic half-life of $\sim 4 \times 10^7\ years$, while for C_{60}^{3-} we estimate a very short half-life of $2.4 \times 10^{-12}\ s$. Both these estimates are in correspondence with observations. Indeed, C_{60}^{3-} has not been observed as a free molecule, while the free C_{60}^{2-} has been observed to be long lived [98, 99] and was detected even 5 *min* after its production through laser vaporization [99].

We note that the WKB lifetimes calculated for tunneling through Coulombic barriers are very sensitive to the final energy of the emitted particle and can vary by many orders of magnitude as a result of small changes in this energy, a feature well known from the alpha radioctivity of nuclei [102].

Since the second electron affinity of C_{60} is small, effects due to geometrical relaxation and spin polarization can influence its value and, consequently, the estimated

lifetime. Nevertheless, as shown in Ref. [95], inclusion of such corrections yields again a negative second affinity, but of somewhat smaller magnitude, resulting in an even longer lifetime (the sign conventions in Ref. [95] are the opposite of ours).

Furthermore, as discussed in Ref. [103], the stabilization effect of the Jahn-Teller relaxation for the singly-charged ion is only of the order of $0.03 - 0.05\ eV$. Since this effect is expected to be largest for singly-charged species, C_{60}^{2-} is not expected to be influenced by it [95].

On the other hand, generalized exchange-correlation functionals with gradient corrections yield slightly larger values for the second electron affinity. For example, using exchange-correlation gradient corrections, Ref. [95] found $A_2^{ico} = -0.3\ eV$, which is higher (in absolute magnitude) than the value obtained without such corrections. This value of $-0.3\ eV$ leads to a much smaller lifetime than the several million of years that correspond to the value of $-0.09\ eV$ calculated by us. Indeed, using the barrier displayed in Fig. 1.11(a), we estimate a lifetime for C_{60}^{2-} of approx. $0.37\ s$, when $A_2^{ico} = -0.3\ eV$. We stress, however, that even this lower-limit value still corresponds to macroscopic times and is 5 orders of magnitude larger than the estimate of Ref. [98], which found a lifetime of $1\ \mu s$ for $A_2^{ico} = -0.3\ eV$, since it omitted the large centrifugal barrier. Indeed, when we omit the centrifugal barrier, we find a lifetime estimate of $1.4\ \mu s$, when $A_2^{ico} = -0.3\ eV$.

1.3.3. *On mesoscopic forces and quantized conductance in model metallic nanowires*

1.3.3.1. *Background and motivation*

In this section, we show that certain aspects of the mechanical response (i.e., elongation force) and electronic transport (e.g., quantized conductance) in metallic nanowires can be analyzed using the DFT shell correction method, developed and applied previously in studies of metal clusters (see Sec. 1.2 and Sec. 1.3.1). Specifically, we show that in a jellium-modelled, volume-conserving nanowire, variations of the total energy (particularly terms associated with electronic subband corrections) upon elongation of the wire lead to *self-selection* of a sequence of stable "magic" wire configurations (MWC's, specified in our model by a sequence of the wire's radii), with the force required to elongate the wire from one configuration to the next exhibiting an oscillatory behavior. Moreover, we show that due to the quantized nature of electronic states in such wires, the electronic conductance varies in a quantized step-wise manner (in units of the conductance quantum $g_0 = 2e^2/h$), correlated with the transitions between MWC's and the above-mentioned force oscillations.

Prior to introducing the model, it is appropriate to briefly review certain previous theoretical and experimental investigations, which form the background and motivation for this study of nanowires. Atomistic descriptions, based on realistic interatomic interactions, and/or first-principles modelling and simulations played

an essential role in discovering the formation of nanowires, and in predicting and elucidating the microscopic mechanisms underlying their mechanical, spectral, electronic and transport properties.

Formation and mechanical properties of interfacial junctions (in the form of crystalline nanowires) have been predicted through early molecular-dynamics simulations [104], where the materials (gold) were modelled using semiempirical embedded-atom potentials. In these studies it has been shown that separation of the contact between materials leads to generation of a connective junction which elongates and narrows through a sequence of structural instabilities; at the early stages, elongation of the junction involves multiple slip events, while at the later stages, when the lateral dimension of the wire necks down to a diameter of about 15 Å, further elongation involves a succession of stress accumulation and fast relief stages associated with a sequence of order-disorder structural transformations localized to the neck region [104–106]. These structural evolution patterns have been shown through the simulations to be portrayed in oscillations of the force required to elongate the wire, with a period approximately equal to the interlayer spacing. In addition, the "saw-toothed" character of the predicted force oscillations (see Fig. 3(b) in Ref. [104] and Fig. 3 in Ref. [105]) reflects the stress accumulation and relief stages of the elongation mechanism. Moreover, the critical resolved yield stress of gold nanowires has been predicted [104, 105] to be ~ 4GPa, which is over an order of magnitude larger than that of the bulk, and is comparable to the theoretical value for Au (1.5 GPa) in the absence of dislocations.

These predictions, as well as anticipated electronic conductance properties [104, 107], have been corroborated in a number of experiments using scanning tunneling and force microscopy [104, 108–113], break junctions [114], and pin-plate techniques [105, 115] at ambient environments, as well as under ultrahigh vacuum and/or cryogenic conditions. Particularly, pertinent to this section are experimental observations of the oscillatory behavior of the elongation forces and the correlations between the changes in the conductance and the force oscillations; see especially the simultaneous measurements of force and conductance in gold nanowires in Ref. [112], where in addition the predicted "ideal" value of the critical yield stress has also been measured (see also Ref. [113]).

The jellium-based model introduced in this paper, which by construction is devoid of atomic crystallographic structure, does not address issues pertaining to nanowire formation methods, atomistic configurations, and mechanical response modes (e.g., plastic deformation mechanisms, interplanar slip, ordering and disordering mechanisms (see detailed descriptions in Refs. [104, 105] and [106], and a discussion of conductance dips in Ref. [110]), defects, mechanichal reversibility [105, 112], and roughening of the wires' morphology during elongation [106]), nor does it consider the effects of the above on the electron spectrum, transport properties, and dynamics [116]. Nevertheless, as shown below, the model offers a useful framework for linking investigations of solid-state structures of reduced

Constantine Yannouleas and Uzi Landman

dimensions (e.g., nanowires) with methodologies developed in cluster physics, as well as highlighting certain nanowire phenomena of mesoscopic origins and their analogies to clusters.

1.3.3.2. *The jellium model for metallic nanowires: Theoretical method and results*

Consider a cylindrical jellium wire of length L, having a positive background with a circular cross section of constant radius $R \ll L$ [117]. For simplicity, we restrict ourselves here to this symmetry of the wire cross section. Variations in the shape of the nanowire cross section serve to affect the degeneracies of the electronic spectrum [118, 119] without affecting our general conclusions. We also do not include here variations of the wire's shape along its axis. Adiabatic variation of the wire's axial shape introduces a certain amount of smearing of the conductance steps through tunnelling, depending on the axial radius of curvature of the wire [118–120]. Both the cross-sectional and axial shape of the wire can be included in our model in a rather straightforward manner.

As elaborated in Sec. 1.2, the principal idea of the SCM is the separation of the total DFT energy $E_T(R)$ of the nanowire as

$$E_T(R) = \widetilde{E}(R) + \Delta E_{sh}(R), \tag{1.46}$$

where $\widetilde{E}(R)$ varies smoothly as a function of the radius R of the wire (instead of the number of electrons N used in Sec. 1.2), and $\Delta E_{sh}(R)$ is the shell-correction term arising from the discrete quantized nature of the electronic levels. Again, as elaborated in Sec. 1.2, the smooth contribution in Eq. (1.46) is identified with $E_{ETF}[\widetilde{\rho}]$. The trial radial lateral density $\widetilde{\rho}(r)$ is given by Eq. (1.25), and the constant ρ_0 at a given radius R is obtained under the normalization condition (charge neutrality) $2\pi \int \widetilde{\rho}(r)rdr = \rho_L^{(+)}(R)$, where $\rho_L^{(+)}(R) = 3R^2/(4r_s^3)$ is the linear positive background density. Using the optimized $\widetilde{\rho}$, one solves for the eigenvalues $\widetilde{\epsilon}_i$ of the Hamiltonian $H = -(\hbar^2/2m)\nabla^2 + V_{ETF}[\widetilde{\rho}]$, and the shell correction is given by

$$\begin{aligned} \Delta E_{sh} &\equiv E_{\text{Harris}}[\widetilde{\rho}] - E_{ETF}[\widetilde{\rho}] \\ &= \sum_{i=1}^{\text{occ}} \widetilde{\epsilon}_i - \int \widetilde{\rho}(\mathbf{r})V_{ETF}[\widetilde{\rho}(\mathbf{r})]d\mathbf{r} - T_{ETF}[\widetilde{\rho}], \end{aligned} \tag{1.47}$$

where the summation extends over occupied levels. Here the dependence of all quantities on the pertinent size variable (i.e., the radius of the wire R) is not shown explicitly. Additionally, the index i can be both discrete and continuous, and in the latter case the summation is replaced by an integral (see below).

Following the above procedure with a uniform background density of sodium ($r_s = 4$ a.u.), a typical potential $V_{ETF}(r)$ for $R = 12.7$ a.u., where r is the radial coordinate in the transverse plane, is shown in Fig. 1.12, along with the transverse eigenvalues $\widetilde{\epsilon}_{nm}$ and the Fermi level; to simplify the calculations of the electronic
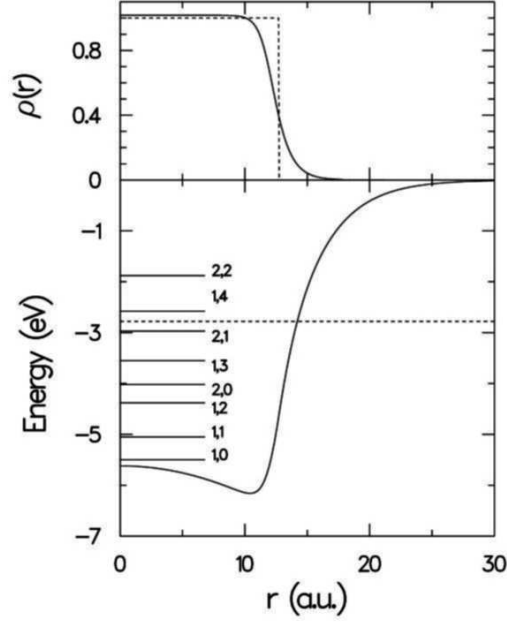
Fig. 1.12.   Lower panel: The $V_{ETF}(r)$ potential for a sodium wire with a uniform jellium background of radius $R = 12.7$ a.u., plotted versus the transverse radial distance from the center of the wire, along with the locations of the bottoms of the subbands (namely the transverse eigenvalues $\widetilde{\epsilon}_{nm}$; n is the number of nodes in the radial direction plus one, and m is the azimuthal quantum number of the angular momentum). The Fermi level is denoted by a dashed line. Top panel: The jellium background volume density (dashed line) and the electronic volume density $\widetilde{\rho}(r)$ (solid line, exhibiting a characteristic spillout) normalized to bulk values are shown.

spectrum, we have assumed (as noted above) $R \ll L$, which allows us to express the subband electronic spectrum as

$$\widetilde{\epsilon}_{nm}(k_z; R) = \widetilde{\epsilon}_{nm}(R) + \frac{\hbar^2 k_z^2}{2m}, \tag{1.48}$$

where k_z is the electron wave number along the axis of the wire (z).

As indicated earlier, taking the wire to be charge neutral, the electronic linear density, $\rho_L^{(--)}(R)$, must equal the linear positive background density, $\rho_L^{(+)}(R)$. The chemical potential (at $T = 0$ the Fermi energy ϵ_F) for a wire of radius R is determined by setting the expression for the electronic linear density derived from the subband spectra equal to $\rho_L^{(+)}(R)$, i.e.,

$$\frac{2}{\pi} \sum_{n,m}^{\mathrm{occ}} \sqrt{\frac{2m}{\hbar^2}[\epsilon_F(R) - \widetilde{\epsilon}_{nm}(R)]} = \rho_L^{(+)}(R), \tag{1.49}$$

where the factor of 2 on the left is due to the spin degeneracy. The summand defines the Fermi wave vector for each subband, $k_{F,nm}$. The resulting variation of $\epsilon_F(R)$ versus R is displayed in Fig. 1.13(a), showing cusps for values of the radius where a
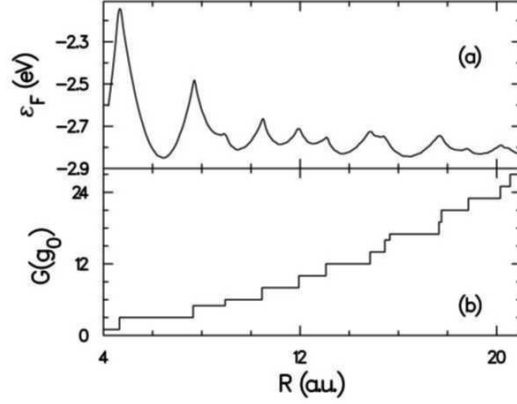
Constantine Yannouleas and Uzi Landman

Fig. 1.13.   Variation of the Fermi energy ϵ_F [shown in (a)] and of the conductance G (shown in (b) in units of $g_0 = 2e^2/h$), plotted versus the radius R, for a sodium nanowire. Note the coincidence of the cusps in ϵ_F with the step-rises of the conductance. The heights of the steps in G reflect the subband degeneracies due to the circular shape of the wire's cross section.

new subband drops below the Fermi level as R increases (or conversely as a subband moves above the Fermi level as R decreases upon elongation of the wire). Using the Landauer expression for the conductance G in the limit of no mode mixing and assuming unit transmission coefficients, $G(R) = g_0 \sum_{n,m} \Theta[\epsilon_F(R) - \widetilde{\epsilon}_{nm}(R)]$, where Θ is the Heaviside step function. The conductance of the nanowire, shown in Fig. 1.13(b), exhibits quantized step-wise behavior, with the step-rises coinciding with the locations of the cusps in $\epsilon_F(R)$, and the height sequence of the steps is $1g_0$, $2g_0$, $2g_0$, $1g_0$, ..., reflecting the circular symmetry of the cylindrical wires' cross sections [107], as observed for sodium nanowires [114]. Solving for $\epsilon_F(R)$ [see Eq. (1.49)], the expression for the sum on the right-hand-side of Eq. (1.47) can be written as

$$\sum_i^{\text{occ}} \widetilde{\epsilon}_i = \frac{2}{\pi} \sum_{n,m}^{\text{occ}} \int_0^{k_{F,nm}} dk_z \widetilde{\epsilon}_{nm}(k_z; R) =$$
$$\frac{2}{3\pi} \sum_{n,m}^{\text{occ}} [\epsilon_F(R) + 2\widetilde{\epsilon}_{nm}(R)] \sqrt{\frac{2m}{\hbar^2}[\epsilon_F(R) - \widetilde{\epsilon}_{nm}(R)]}, \qquad (1.50)$$

which allows one to evaluate ΔE_{sh} [Eq. (1.47)] for each wire radius R. Since the expression in Eq. (1.50) gives the energy per unit length, we also calculate E_{ETF}, T_{ETF}, and the volume integral in the second line of Eq. (1.47) for cylindrical volumes of unit height. To convert to energies per unit volume [denoted as $\varepsilon_T(R)$, $\widetilde{\varepsilon}(R)$, and $\Delta\varepsilon_{sh}(R)$] all energies are further divided by the wire's cross-sectional area, πR^2. The smooth contribution and the shell correction to the wire's energy are shown respectively in Fig. 1.14(a) and Fig. 1.14(b). The smooth contribution decreases slowly towards the bulk value (-2.25 eV per atom [3]). On the other hand, the
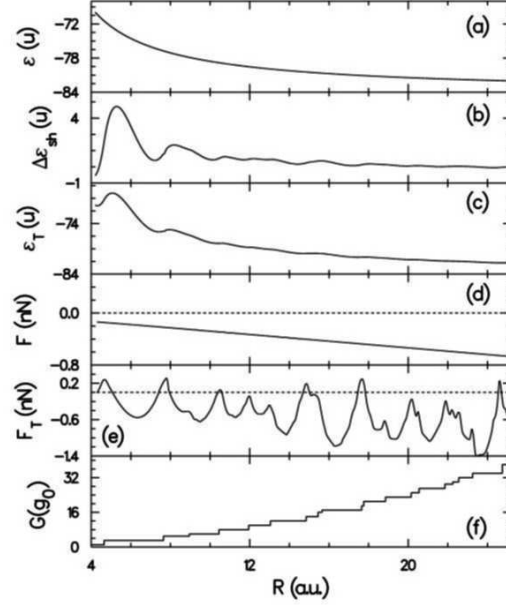
Fig. 1.14.   (a-c): The smooth (a) and shell-correction (b) contributions to the total energy (c) per unit volume of the jellium-modelled sodium nanowire (in units of $u \equiv 10^{-4}$ eV/a.u.^{3}), plotted versus the radius of the wire (in a.u.). Note the smaller magnitude of the shell corrections relative to the smooth contribution. (d-e): The smooth contribution (d) to the total force and the total force (e), plotted in units of nN versus the wire's radius. In (e), the zeroes of the force to the left of the force maxima occur at radii corresponding to the local minima of the energy of the wire (c). In (f), we reproduce the conductance of the wire (in units of $g_0 = 2e^2/h$), plotted versus R. Interestingly, calculations of the conductance for the MWC's (i.e., the wire radii corresponding to the locations of the step-rises) through the Sharvin-Weyl formula, [119, 121] corrected for the finite height of the confining potential [121] (see lower panel of Fig. 1.12), namely $G = g_0(\pi S/\lambda_F^2 - \alpha P/\lambda_F)$ where S and P are the area and perimeter of the wire's cross section and λ_F is the Fermi wavelength ($\lambda_F = 12.91$ a.u. for Na) with $\alpha = 0.1$ (see Ref. [121]), yield results which approximate well the conductance values (i.e., the values at the bottom of the step-rises) shown in (f).

shell corrections are much smaller in magnitude and exhibit an oscillatory behavior. This oscillatory behavior remains visible in the total energy [Fig. 1.14(c)] with the local energy minima occurring for values $R_{\min}$ corresponding to conductance plateaus. The sequence of $R_{\min}$ values defines the MWC's, that is a sequence of wire configurations of enhanced stability.

From the expressions for the total energy of the wire [i.e., $\Omega\varepsilon_T(R)$, where $\Omega = \pi R^2 L$ is the volume of the wire] and the smooth and shell (subband) contributions to it, we can calculate the "elongation force" (EF),

$$F_T(R) = -\frac{d[\Omega\varepsilon_T(R)]}{dL} = -\Omega\left\{\frac{d\widetilde{\varepsilon}(R)}{dL} + \frac{d[\Delta\varepsilon_{sh}(R)]}{dL}\right\}$$
$$\equiv \widetilde{F}(R) + \Delta F_{sh}(R). \tag{1.51}$$

Using the volume conservation, i.e., $d(\pi R^2 L) = 0$, these forces can be written as $F_T(R) = (\pi R^3/2)d\varepsilon_T(R)/dR$, $\widetilde{F}(R) = (\pi R^3/2)d\widetilde{\varepsilon}(R)/dR$, and $\Delta F_{sh}(R) = (\pi R^3/2)d[\Delta\varepsilon_{sh}(R)]/dR$. $\widetilde{F}(R)$ and $F_T(R)$ are shown in Fig. 1.14(d,e). The oscillations in the force resulting from the shell-correction contributions dominate. In all cases, the radii corresponding to zeroes of the force situated on the left of the force maxima coincide with the minima in the potential energy curve of the wire, corresponding to the MWC's. Consequently, these forces may be interpreted as guiding the self-evolution of the wire toward the MWC's. Also, all the local maxima in the force occur at the locations of step-rises in the conductance [reproduced in Fig. 1.14(f)], signifying the sequential decrease in the number of subbands below the Fermi level (conducting channels) as the wire narrows (i.e., as it is being elongated). Finally the magnitude of the total forces is comparable to the measured ones (i.e., in the nN range).

1.4. Summary

While it was understood rather early that the total energy of nuclei can be decomposed into an oscillatory part and one that shows a slow "smooth" variation as a function of size, Strutinsky's seminal contribution [1] was to calculate the two parts from different nuclear models: the former from the nuclear shell model and the latter from the liquid drop model. In particular, the calculation of the oscillatory part (shell correction term) was enabled by employing an averaging method that smeared the single particle spectrum associated with a nuclear model potential.

A semiempirical shell-correction method (referred to as SE-SCM) for metal clusters, that was developed in close analogy to the original phenomenological Strutinsky approach, was presented in the Appendix, along with some applications to triaxial deformations and fission barriers of metal clusters.

This chapter reviewed primarily the motivation and theory of a microscopic shell correction method based on density functional theory (often referred to as DFT-SCM and originally introduced in Ref. [3]). In developing the DFT-SCM, we have used for the shell correction term (arising from quantum interference effects) a derivation that differs from the Strutinsky methodology [1]. Instead, we have shown [3] that the shell correction term can be introduced through a kinetic-energy-type density functional [see Eq. (1.19) and Eq. (1.23)].

The DFT-SCM is computationally advantageous, since it bypasses the self-consistent iteration cycle of the more familiar KS-DFT. Indeed, the DFT-SCM energy functional depends only on the single-particle density, and thus it belongs to the class of orbital-free DFT methods. Compared to previous OF-DFT approaches, the DFT-SCM represents an improvement in accuracy.

Applications of the DFT-SCM to condensed-matter nanostructures, and in particular metal clusters, fullerenes, and nanowires, were presented in Sec. 1.3.

Acknowledgements

Appendix A. Semi-empirical shell-correction method (SE-SCM)

As mentioned above already [see, e.g., Sec. 1.1.1], rather than proceed with the microscopic route, Strutinsky proposed a method for separation of the total energy into smooth and shell-correction terms [see Eq. (1.1)] based on an averaging procedure. Accordingly, a smooth part, $\widetilde{E}_{sp}$, is extracted out of the sum of the single-particle energies $\sum_i \widetilde{\varepsilon}_i$ [see Eq. (1.6), or equivalently Eq. (1.16) with ρ^{in} replaced by $\widetilde{\rho}$ and $\varepsilon_i^{\mathrm{out}}$ by $\widetilde{\varepsilon}_i$] by averaging them through an appropriate procedure. Usually, but not necessarily, one replaces the delta functions in the single-particle density of states by gaussians or other appropriate weighting functions. As a result, each single-particle level is assigned an averaging occupation number $\widetilde{f}_i$, and the smooth part $\widetilde{E}_{sp}$ is formally written as

$$\widetilde{E}_{sp} = \sum_i \widetilde{\varepsilon}_i \widetilde{f}_i. \tag{A.1}$$

Consequently, the Strutinsky shell correction is given by

$$\Delta E_{sh}^{Str} = \sum_{i=1}^{\mathrm{occ}} \widetilde{\varepsilon}_i - \widetilde{E}_{sp}. \tag{A.2}$$

The Strutinsky prescription (A.2) has the practical advantage of using only the single-particle energies $\widetilde{\varepsilon}_i$, and not the smooth density $\widetilde{\rho}$. Taking advantage of this, the single-particle energies can be taken as those of an external potential that empirically approximates the self-consistent potential of a finite system. In the nuclear case, an anisotropic three-dimensional harmonic oscillator has been used successfully to describe the shell-corrections in deformed nuclei.

The single-particle smooth part, $\widetilde{E}_{sp}$, however, is only one component of the total smooth contribution, $\widetilde{E}[\widetilde{\rho}]$ ($\widetilde{E}_{HF}$ in the Hartree-Fock energy considered by Strutinsky). Indeed as can be seen from Eq. (1.6) [or equivalently Eq. (1.16)],

$$E_{\mathrm{total}} \approx \Delta E_{sh}^{Str} + \widetilde{E}[\widetilde{\rho}]. \tag{A.3}$$

Strutinsky did not address the question of how to calculate microscopically the smooth part $\widetilde{E}$ (which necessarily entails specifying the smooth density $\widetilde{\rho}$). Instead he circumvented this question by substituting for $\widetilde{E}$ the empirical energies, E_{LDM}, of the nuclear liquid drop model, namely he suggested that

$$E_{\mathrm{total}} \approx \Delta E_{sh}^{Str} + E_{LDM}. \tag{A.4}$$

In applications of Eq. (A.4), the single-particle energies involved in the averaging [see Eqs. (A.1) and (A.2)] are commonly obtained as solutions of a Schrödinger equation with phenomenological one-body potentials. This last approximation has been

very successful in describing fission barriers and properties of strongly deformed nuclei using harmonic oscillator or Wood-Saxon empirical potentials.

In the following (Sec. A.1), we describe the adaptation of the SE-SCM approach to condensed-matter finite systems, and in particular to triaxially deformed metal clusters. Moreover (Sec. A.2), we will present several figures illustrating applications of the SE-SCM to investigations of the effects of triaxial shape-deformations on the properties of metal clusters [25, 33, 35–37] and to studies of large-scale deformations and barriers in fission of charged metal clusters [26, 27, 38]. We note that the SE-SCM has been extended to incorporate electronic entropy effects at finite temperatures. This latter extension, referred to as finite-temperature (FT)-SE-SCM is not described here, but its theory can be found in Ref. [33].

We mention that, in addition, Strutinsky-type calculations using phenomenological potentials have been reported for the case of neutral sodium clusters assuming axial symmetry in Refs. [29–31, 122], and for the case of fission in Ref. [28].

A.1. Semiempirical shell-correction method for triaxially deformed clusters

A.1.1. *Liquid-drop model for neutral and charged deformed clusters*

For neutral clusters, the liquid-drop model [28, 48, 123] (LDM) expresses the *smooth* part, $\widetilde{E}$, of the total energy as the sum of three contributions, namely a volume, a surface, and a curvature term, i.e.,

$$\widetilde{E} = E_{vol} + E_{surf} + E_{curv} =$$
$$A_v \int d\tau + \sigma \int dS + A_c \int dS\kappa, \tag{A.5}$$

where $d\tau$ is the volume element and dS is the surface differential element. The local curvature κ is defined by the expression $\kappa = 0.5(R_{max}^{-1} + R_{min}^{-1})$, where R_{max} and R_{min} are the two principal radii of curvature at a local point on the surface of the jellium droplet which models the cluster. The corresponding coefficients can be determined by fitting the extended Thomas-Fermi (ETF)-DFT total energy $E_{ETF}[\rho]$ (see Sec. 1.2.2) for spherical shapes to the following parametrized expression as a function of the number, N, of atoms in the cluster [124],

$$E_{ETF}^{sph} = \alpha_v N + \alpha_s N^{2/3} + \alpha_c N^{1/3}. \tag{A.6}$$

The following expressions relate the coefficients A_v, σ, and A_c to the corresponding coefficients, (α's), in Eq. (A.6),

$$A_v = \frac{3}{4\pi r_s^3}\alpha_v \; ; \; \sigma = \frac{1}{4\pi r_s^2}\alpha_s \; ; \; A_c = \frac{1}{4\pi r_s}\alpha_c. \tag{A.7}$$

In the case of ellipsoidal shapes the areal integral and the integrated curvature can be expressed in closed analytical form with the help of the incomplete elliptic integrals $\mathcal{F}(\psi, k)$ and $\mathcal{E}(\psi, k)$ of the first and second kind [125], respectively. Before

Shell-correction and orbital-free density-functional methods for finite systems   37

writing the formulas, we need to introduce some notations. Volume conservation must be employed, namely

$$a'b'c'/R_0^3 = abc = 1, \tag{A.8}$$

where R_0 is the radius of a sphere with the same volume ($R_0 = r_s N^{1/3}$ is taken to be the radius of the positive jellium assuming spherical symmetry), and $a = a'/R_0$, etc..., are the dimensionless semi-axes. The eccentricities are defined through the dimensionless semi-axes as follows

$$
\begin{aligned}
e_1^2 &= 1 - (c/a)^2 \\
e_2^2 &= 1 - (b/a)^2 \\
e_3^2 &= 1 - (c/b)^2.
\end{aligned}
\tag{A.9}
$$

The semi-axes are chosen so that

$$a \geq b \geq c. \tag{A.10}$$

With the notation $\sin\psi = e_1$, $k_2 = e_2/e_1$, and $k_3 = e_3/e_1$, the relative (with respect to the spherical shape) surface and curvature energies are given [126] by

$$\frac{E_{surf}^{ell}}{E_{surf}^{sph}} = \frac{ab}{2}\left[\frac{1-e_1^2}{e_1}\mathcal{F}(\psi,k_3) + e_1\mathcal{E}(\psi,k_3) + c^3\right] \tag{A.11}$$

and

$$\frac{E_{curv}^{ell}}{E_{curv}^{sph}} = \frac{bc}{2a}\left[1 + \frac{a^3}{e_1}\left((1-e_1^2)\mathcal{F}(\psi,k_2) + e_1^2\mathcal{E}(\psi,k_2)\right)\right]. \tag{A.12}$$

The change in the smooth part of the cluster total energy due to the excess charge $\pm Z$ was already discussed by us for spherical clusters in the previous section. The result may be summarized as

$$\Delta\widetilde{E}^{sph}(Z) = \widetilde{E}^{sph}(Z) - \widetilde{E}^{sph}(0) = \mp WZ + \frac{Z(Z \pm 0.25)e^2}{2(R_0 + \delta)}, \tag{A.13}$$

where the upper and lower signs correspond to negatively and positively charged states, respectively, W is the work function of the metal, R_0 is the radius of the positive jellium assuming spherical symmetry, and δ is a spillout-type parameter.

To generalize the above results to an ellipsoidal shape, $\phi(R_0 + \delta) = e^2/(R_0 + \delta)$, which is the value of the potential on the surface of a spherical conductor, needs to be replaced by the corresponding expression for the potential on the surface of a conducting ellipsoid. The final result, normalized to the spherical shape, is given by the expression

$$\frac{\Delta\widetilde{E}^{ell}(Z) \pm WZ}{\Delta\widetilde{E}^{sph}(Z) \pm WZ} = \frac{bc}{e_1}\mathcal{F}(\psi,k_2), \tag{A.14}$$

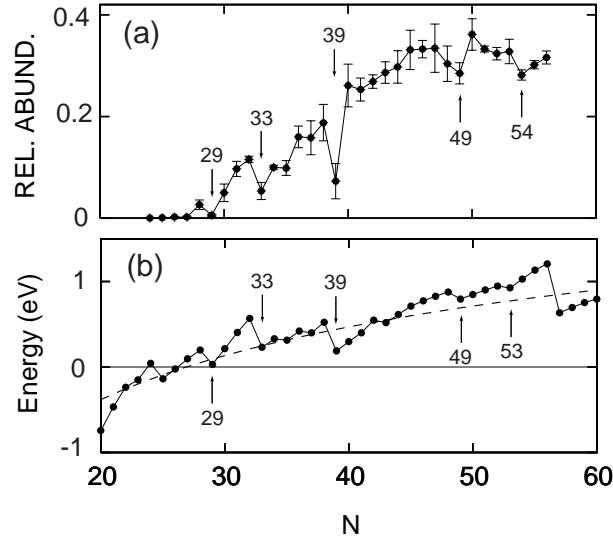where the $\pm$ sign in front of WZ corresponds to negatively and positively charged clusters, respectively.

38   *Constantine Yannouleas and Uzi Landman*

Fig. A.1.   (a) Experimental yields (denoted as "REL. ABUND.") of dianionic silver clusters Ag_N^{2-}, plotted versus cluster size. The error bars indicate the statistical uncertainty. (b) Theoretical FT-SE-SCM [33] second electron affinities A_2 for Ag_N^{2-} clusters at $T = 300$ K. LDM results are depicted by the dashed line. The figure was reproduced from Ref. [36].

A.1.2. *The modified Nilsson potential*

A natural choice for an external potential to be used for calculating shell corrections with the Strutinsky method is an anisotropic, three-dimensional oscillator with an $\mathbf{l}^2$ term for lifting the harmonic oscillator degeneracies [127]. Such an oscillator model for approximating the total energies of metal clusters, but without separating them into a smooth and a shell-correction part in the spirit of Strutinsky' s approach, has been used [58] with some success for calculating relative energy surfaces and deformation shapes of metal clusters. However, this simple harmonic oscillator model has serious limitations, since i) the total energies are calculated by the expression $\frac{3}{4}\sum_i \varepsilon_i$, and thus do not compare with the total energies obtained from the KS-DFT approach, ii) the model cannot be extended to the case of charged (cationic or anionic) clusters. Thus absolute ionization potentials, electron affinities, and fission energetics cannot be calculated in this model. Alternatively, in our approach, we are making only a limited use of the external oscillator potential in calculating a modified Strutinsky shell correction. Total energies are evaluated by adding this shell correction to the smooth LDM energies.

In particular, a modified Nilsson Hamiltonian appropriate for metal clusters [128, 129] is given by

$$H_N = H_0 + U_0\hbar\omega_0(\mathbf{l}^2 - <\mathbf{l}^2>_n), \tag{A.15}$$

where H_0 is the hamiltonian for a three-dimensional anisotropic oscillator, namely

$$H_0 = -\frac{\hbar^2}{2m_e}\triangle + \frac{m_e}{2}(\omega_1^2 x^2 + \omega_2^2 y^2 + \omega_3^2 z^2) =$$

$$\sum_{k=1}^{3}(a_k^\dagger a_k + \frac{1}{2})\hbar\omega_k. \tag{A.16}$$

U_0 in Eq. (A.15) is a dimensionless parameter, which for occupied states may depend on the principal quantum number $n = n_1 + n_2 + n_3$ of the spherical-oscillator major shell associated with a given level (n_1, n_2, n_3) of the hamiltonian H_0 (for clusters comprising up to 100 valence electrons, only a weak dependence on n is found, see Table I in Ref. [25]). U_0 vanishes for values of n higher than the corresponding value of the last partially (or fully) filled major shell in the spherical limit.

$\mathbf{l}^2 = \sum_{k=1}^{3} l_k^2$ is a "stretched" angular momentum which scales to the ellipsoidal shape and is defined as follows,

$$l_3^2 \equiv (q_1 p_2 - q_2 p_1)^2, \tag{A.17}$$

(with similarly obtained expressions for l_1 and l_2 via a cyclic permutation of indices) where the stretched position and momentum coordinates are defined via the corresponding natural coordinates, q_k^{nat} and p_k^{nat}, as follows,

$$q_k \equiv q_k^{nat}(m_e\omega_k/\hbar)^{1/2} = \frac{a_k^\dagger + a_k}{\sqrt{2}} \ , \ (k = 1, 2, 3), \tag{A.18}$$

$$p_k \equiv p_k^{nat}(1/\hbar m_e\omega_k)^{1/2} = i\frac{a_k^\dagger - a_k}{\sqrt{2}} \ , \ (k = 1, 2, 3). \tag{A.19}$$

The stretched $\mathbf{l}^2$ is not a properly defined angular-momentum operator, but has the advantageous property that it does not mix deformed states which correspond to sherical major shells with different principal quantum number $n = n_1 + n_2 + n_3$ (see, the appendix in Ref. [25] for the expression of the matrix elements of $\mathbf{l}^2$).

The subtraction of the term $< \mathbf{l}^2 >_n = n(n + 3)/2$, where $< >_n$ denotes the expectation value taken over the nth-major shell in spherical symmetry, guaranties that the average separation between major oscillator shells is not affected as a result of the lifting of the degeneracy.

The oscillator frequencies can be related to the principal semi-axes a', b', and c' [see Eq. (A.8)] via the volume-conservation constraint and the requirement that the surface of the cluster is an equipotential one, namely

$$\omega_1 a' = \omega_2 b' = \omega_3 c' = \omega_0 R_0, \tag{A.20}$$

where the frequency ω_0 for the spherical shape (with radius R_0) was taken according to Ref. [130] to be

$$\hbar\omega_0(N) = \frac{49 \text{ eV bohr}^2}{r_s^2 N^{1/3}}\left[1 + \frac{t}{r_s N^{1/3}}\right]^{-2}. \tag{A.21}$$
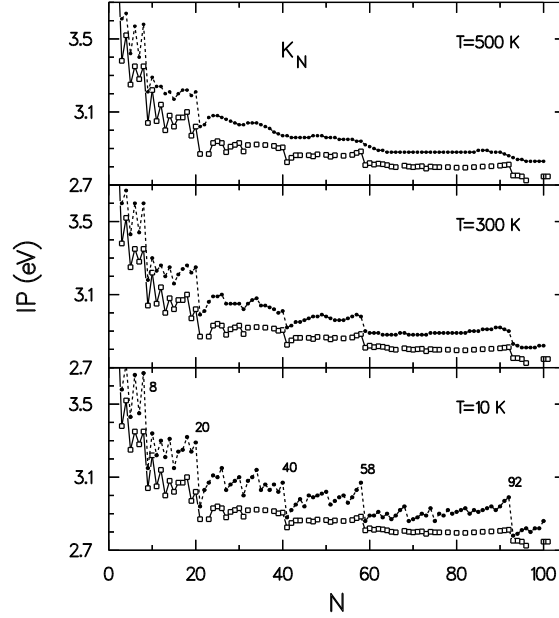
Fig. A.2.   Ionization potentials of neutral K_N clusters at three temperatures, $T = 10$, 300, and 500 K. Solid dots: theoretical FT-SE-SCM [33] results. Open squares: experimental measurements [129]. The best agreement between theory and experiment happens for $T = 300$ K (room temperature), indicating the importance of the electronic entropy in quenching the shell effects.

Since in this paper we consider solely monovalent elements, N in Eq. (A.21) is the number of atoms for the family of clusters $M_N^{Z\pm}$, r_s is the Wigner-Seitz radius expressed in atomic units, and t denotes the electronic spillout for the neutral cluster according to Ref. [130].

A.1.3.   *Averaging of single-particle spectra and semi-empirical shell correction*

Usually $\widetilde{E}_{sp}$ [see Eqs. (A.1) and (A.2)] is calculated numerically [131]. However, a variation of the numerical Strutinsky averaging method consists in using the semiclassical partition function and in expanding it in powers of $\hbar^2$. With this method, for the case of an anisotropic, fully triaxial oscillator, one finds [43, 132] an analytical result, namely [133]

$$\widetilde{E}_{sp}^{osc} = \hbar(\omega_1\omega_2\omega_3)^{1/3}$$
$$\times \left(\frac{1}{4}(3N_e)^{4/3} + \frac{1}{24}\frac{\omega_1^2 + \omega_2^2 + \omega_3^2}{(\omega_1\omega_2\omega_3)^{2/3}}(3N_e)^{2/3} \right), \qquad (A.22)$$

where N_e denotes the number of delocalized valence electrons in the cluster.

In the present work, expression (A.22) (as modified below) will be substituted for the average part $\widetilde{E}_{sp}$ in Eq. (A.2), while the sum $\sum_i^{\text{occ}} \varepsilon_i$ will be calculated numerically by specifying the occupied single-particle states of the modified Nilsson oscillator represented by the hamiltonian (A.15).

In the case of an isotropic oscillator, not only the smooth contribution, $\widetilde{E}_{sp}^{osc}$, but also the Strutinsky shell correction (A.2) can be specified analytically, [43] with the result

$$\Delta E_{sh,0}^{Str}(x) = \frac{1}{24}\hbar\omega_0(3N_e)^{2/3}(-1 + 12x(1-x)), \tag{A.23}$$

where x is the fractional filling of the highest partially filled harmonic oscillator shell. For a filled shell ($x = 0$), $\Delta E_{sh,0}^{Str}(0) = -\frac{1}{24}\hbar\omega_0(3N_e)^{2/3}$, instead of the essentially vanishing value as in the case of the ETF-DFT defined shell correction (cf. Fig. 1 of Ref. [25]). To adjust for this discrepancy, we add $-\Delta E_{sh,0}^{Str}(0)$ to ΔE_{sh}^{Str} calculated through Eq. (A.2) for the case of open-shell, as well as closed-shell clusters.

A.1.4.   *Overall procedure*

We are now in a position to summarize the calculational procedure, which consists of the following steps:

(1) Parametrize results of ETF-DFT calculations for spherical neutral jellia according to Eq. (A.6).
(2) Use above parametrization (assuming that parameters per differential element of volume, surface, and integrated curvature are shape independent) in Eq. (A.5) to calculate the liquid-drop energy associated with neutral clusters, and then add to it the charging energy according to Eq. (A.14) to determine the total LDM energy $\widetilde{E}$.
(3) Use Equations (A.15) and (A.16) for a given deformation [i.e., a', b', c', or equivalently ω_1, ω_2, ω_3, see Eq. (A.20)] to solve for the single-particle spectrum (ε_i).
(4) Evaluate the average, $\widetilde{E}_{sp}$, of the single-particle spectrum according to Eq. (A.22) and subsequent remarks.
(5) Use the results of steps 3 and 4 above to calculate the shell correction ΔE_{sh}^{Str} according to Eq. (A.2).
(6) Finally, calculate the total energy E_{sh} as the sum of the liquid-drop contribution (step 2) and the shell correction (step 5), namely $E_{sh} = \widetilde{E} + \Delta E_{sh}^{Str}$.

The optimal ellipsoidal geometries for a given cluster $M_N^{Z\pm}$, neutral or charged, are determined by systematically varying the distortion (namely, the parameters a and b) in order to locate the global minimum of the total energy $E_{sh}(N, Z)$.
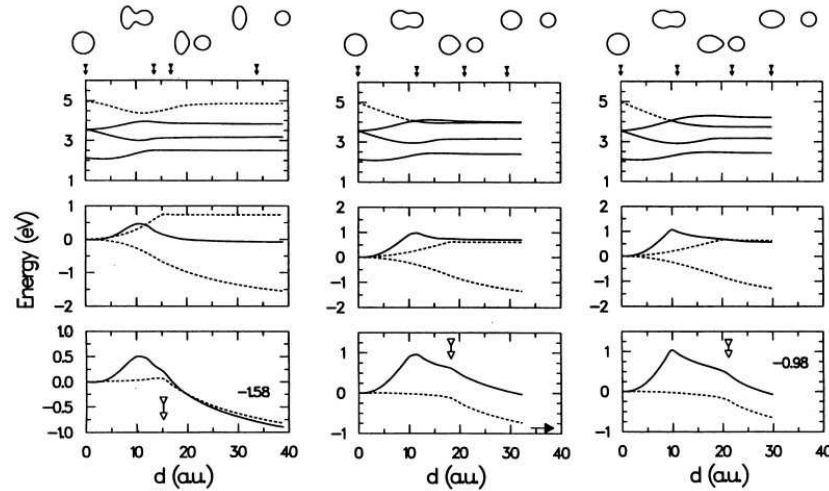
42   *Constantine Yannouleas and Uzi Landman*

Fig. A.3.   Two-center-oscillator [26, 27] SE-SCM results for the asymmetric channel $Na_{10}^{2+} \rightarrow$ $Na_7^+ + Na_3^+$. The final configuration of Na_3^+ is spherical. For the heavier fragment Na_7^+, we present results associated with three different final shape configurations, namely, oblate [(o,s); left], spherical [(s,s); middle], and prolate [(p,s); right]. The ratio of shorter over longer axis is 0.555 for the oblate case and 0.75 for the prolate case.
Bottom panel: LDM energy (surface plus Coulomb, dashed curve) and total potential energy (LDM plus shell corrections, solid curve) as a function of fragment separation d. The empty vertical arrow marks the scission point. The zero of energy is taken at $d = 0$. A number (-1.58 eV or -0.98 eV), or a horizontal solid arrow, denotes the corresponding dissociation energy.
Middle panel: Shell-correction contribution (solid curve), surface contribution (upper dashed curve), and Coulomb contribution (lower dashed curve) to the total energy, as a function of fragment separation d.
Top panel: Single-particle spectra as a function of fragment separation d. The occupied (fully or partially) levels are denoted with solid lines. The unoccupied levels are denoted with dashed lines. On top of the figure, four snapshots of the evolving cluster shapes are displayed. The solid vertical arrows mark the corresponding fragment separations. Observe that the doorway molecular configurations correspond to the second snapshot from the left. Notice the change in energy scale for the middle and bottom panels, as one passes from (o,s) to (s,s) and (p,s) final configurations.

A.2. Applications of SE-SCM to metal clusters

As examples of applications of the SE-SCM, we present here three cases. In Fig. A.1, we show experimental electron affinities for doubly negatively charged silver clusters [134] and compare them with theoretical calculations [36]. In Fig. A.2, we compare FT-SE-SCM calculations for the IPs of neutral K_N clusters with experimental results [33]; such comparisons demonstrate the importance of electronic-entropy effects. Finally, in Fig. A.3, we display SE-SCM calculations for the fission barriers associated with the asymmetric channel $Na_{10}^{2+} \rightarrow Na_7^+ + Na_3^+$ [26, 27]; see caption for details. The phenomenological binding potential as a function of fission-fragment separation is described via a two-center-oscillator model [26, 27, 135].

A fourth application of the SE-SCM describing the IPs of triaxially deformed cold sodium clusters was already used in the introductory Sec. 1.1.2 [see Fig. 1.1(c)].

References

[1] V. M. Strutinsky, *Nucl. Phys. A* **95**, 420 (1967); *Nucl. Phys. A* **122**, 1 (1968).

[2] P. Ring and P. Schuck, *The Nuclear Many-Body Problem*, (Springer, New York, 1980).

[3] C. Yannouleas and U. Landman, *Phys. Rev. B* **48**, 8376 (1993).

[4] L. W. Wang and M. P. Teter, *Phys. Rev. B* **45**, 13196 (1992).

[5] F. Perrot, *J. Phys.: Cond. Matter* **6**, 431 (1994).

[6] E. Smargiassi and P. A. Madden, *Phys. Rev. B* **49**, 5220 (1994).

[7] T. J. Frankcombe, G.-J. Kroes, N. I. Choly, and E. Kaxiras, *J. Phys. Chem. B* **109**, 16554 (2005).

[8] Y. A. Wang and E. A. Carter, in *Theoretical Methods in Condensed Phase Chemistry*, S. D. Schwartz (ed.), (Kluwer, Dordrecht, 2000), p. 117.

[9] S. B. Trickey, V. V. Karasiev, and R. S. Jones, *Int. J. Quantum Chem.* **109**, 2943 (2009).

[10] M. Brack, in *Atomic Clusters and Nanoparticles: Les Houches Session LXXIII 2-28 July 2000*, C. Guest, P. Hobza, F. Spiegelman, and F. David (eds.), (Springer, Berlin, 2001) p. 161.

[11] D. Ullmo, T. Nagano, S. Tomsovic, and H. U. Baranger, *Phys. Rev. B* **63**, 125339 (2001).

[12] Ya. I. Delchev, A. I. Kuleff, T. Z. Mineva, F. Zahariev, and J. Maruani, *Int. J. Quantum Chem.* **99**, 265 (2004).

[13] W. Zhu, S. B. Trickey, *Int. J. Quantum Chem.* **100**, 245 (2004). This paper studied a perturbative DFT approach in the context of the Harris functional [62].

[14] W. D. Knight, K. Clemenger, W. A. de Heer, W. A. Saunders, M. Y. Chou, and M. L. Cohen, *Phys. Rev. Lett.* **52**, 2141 (1984).

[15] W. A. de Heer, *Rev. Mod. Phys.* **65**, 611 (1993).

[16] M. Brack, *Rev. Mod. Phys.* **65**, 677 (1993).

[17] M. L. Homer, E. C. Honea, J. L. Persson, and R. L. Whetten, (unpublished).

[18] *Metal Clusters*, W. Ekardt (ed.), (John-Wiley, New York, 1999).

[19] B. J. Zhou and Y. A. Wang, *J. Chem. Phys.* **127**, 064101 (2007).

[20] B. J. Zhou and Y. A. Wang, *J. Chem. Phys.* **128**, 084101 (2008).

[21] U. Landman, R. N. Barnett, C. L. Cleveland, and G. Rajagopal, in *Physics and Chemistry of Finite Systems: From Clusters to Crystals*, P. Jena, S. N. Khanna, and B. K. Rao (eds.), (Kluwer Academic Publishers, Dordrecht, 1992), Vol. I, p. 165; J. Jortner, *Z. Phys. D* **24**, 247 (1992).

[22] M. A. Preston and R. K. Bhaduri, *Structure of the Nucleus*, (Addison-Wesley, London, 1975).

[23] C. Yannouleas and U. Landman, *Chem. Phys. Lett.* **210**, 437 (1993).

[24] R. N. Barnett, C. Yannouleas, and U. Landman, *Z. Phys. D* **26**, 119 (1993).

[25] C. Yannouleas and U. Landman, *Phys. Rev. B* **51**, 1902 (1995).

[26] C. Yannouleas, R. N. Barnett, and U. Landman, *Comments At. Mol. Phys.* **31**, 445 (1995).

[27] C. Yannouleas and U. Landman, *J. Phys. Chem.* **99**, 14577 (1995).

[28] H. Koizumi, S. Sugano, and Y. Ishii, *Z. Phys. D* **28**, 223 (1993); M. Nakamura, Y. Ishii, A. Tamura, and S. Sugano, *Phys. Rev. A* **42**, 2267 (1990).

[29] A. Bulgac and C. Lewenkopf, *Phys. Rev. Lett.* **71**, 4130 (1993).

[30] S. Frauendorf and V. V. Pashkevich, *Z. Phys. D* **26**, S 98 (1993).

[31] S. M. Reimann, M. Brack, and K. Hansen, *Z. Phys. D* **28**, 235 (1993).

[32] C. Yannouleas and U. Landman, *J. Chem. Phys.* **107**, 1032 (1997).

44   *Constantine Yannouleas and Uzi Landman*

[33] C. Yannouleas and U. Landman, *Phys. Rev. Lett.* **78**, 1424 (1997).

[34] C. Yannouleas, U. Landman, and R. N. Barnett, *Dissociation, Fragmentation and Fission of Simple Metal Clusters*, p. 145 in Ref. [18].

[35] C. Yannouleas and U. Landman, *Rhys. Rev. B* **61**, R10587 (2000).

[36] C. Yannouleas, U. Landman, A. Herlert, and L. Schweikhard, *Phys. Rev. Lett.* **86**, 2996 (2001).

[37] C. Yannouleas, U. Landman, A. Herlert, and L. Schweikhard, *Eur. Phys. J. D* **16**, 81 (2001).

[38] C. Yannouleas, U. Landman, C. Brechignac, Ph. Cahuzac, B. Concina, and J. Leygnier, *Phys. Rev. Lett.* **89**, 173403 (2002).

[39] C. Yannouleas and U. Landman, *Chem. Phys. Lett.* **217**, 175 (1994).

[40] C. Yannouleas and U. Landman, *J. Phys. Chem. B* **101**, 5780 (1997).

[41] C. Yannouleas, E. N. Bogachek, and U. Landman, *Phys. Rev. B* **57**, 4872 (1998).

[42] A. Stafford, D. Baeriswyl, and J. Bürki, *Phys. Rev. Lett.* **79**, 2863 (1997).

[43] Å. Bohr and B. R. Mottelson, *Nuclear Structure* (Benjamin, Reading, Massachusetts, 1975), Vol. II.

[44] C. F. Von Weizsäcker, *Z. Phys.* **96**, 431 (1935).

[45] H. A. Bethe and R. F. Bacher, *Rev. Mod. Phys.* **8**, 82 (1936).

[46] W. D. Myers and W. J. Swiatecki, *Nucl. Phys.* **81**, 1 (1966).

[47] D. R. Snider and R. S. Sorbello, *Solid State Commun.* **47**, 845 (1983).

[48] M. Brack, *Phys. Rev. B* **39**, 3533 (1989).

[49] Ll. Serra, F. Garcías, M. Barranco, J. Navarro, L. C. Balbás, and A. Mañanes, *Phys. Rev. B* **39**, 8247 (1989).

[50] M. Membrado, A. F. Pacheco, and J. Sanũdo, *Phys. Rev. B* **41**, 5643 (1990).

[51] E. Engel and J. P. Perdew, *Phys. Rev. B* **43**, 1331 (1991).

[52] M. Seidl, K.-H. Meiwes-Broer, and M. Brack, *J. Chem. Phys.* **95**, 1295 (1991).

[53] C. Yannouleas, R. A. Broglia, M. Brack, and P. F. Bortignon, *Phys. Rev. Lett.* **63**, 255 (1989).

[54] C. Yannouleas and R. A. Broglia, *Phys. Rev. A* **44**, 5793 (1991); *Europhys. Lett.* **15**, 843 (1991); C. Yannouleas, P. Jena, and S. N. Khanna, *Phys. Rev. B* **46**, 9751 (1992).

[55] C. Yannouleas, *Chem. Phys. Lett.* **193**, 587 (1992).

[56] C. Yannouleas and R. A. Broglia, *Ann. Phys.* (N.Y.) **217**, 105 (1992); C. Yannouleas, E. Vigezzi, and R. A. Broglia, *Phys. Rev. B* **47**, 9849 (1993); C. Yannouleas, F. Catara, and N. Van Giai, *Phys. Rev. B* **51**, 4569 (1995).

[57] W. Kohn and L. J. Sham, *Phys. Rev.* **140**, A1133 (1965).

[58] W. A. De Heer, *Rev. Mod. Phys.* **65**, 611 (1993).

[59] V. V. Kresin, *Phys. Rep.* **220**, 1 (1992).

[60] W. Ekardt, W. *Phys. Rev. B* **31**, 6360 (1985).

[61] D. E. Beck, (1991) *Phys. Rev. B* **43**, 7301 (1991).

[62] J. Harris, *Phys. Rev. B* **31**, 1770 (1985).

[63] M. W. Finnis, *J. Phys.: Condens. Matter* **2**, 331 (1990).

[64] H. M. Polatoglou and M. Methfessel, *Phys. Rev. B* **37**, 10403 (1988).

[65] W. M. C. Foulkes and R. Haydock, *Phys. Rev. B* **39**, 12520 (1989).

[66] E. Zaremba, *J. Phys.: Condens. Matter* **2**, 2479 (1990).

[67] L. H. Thomas, *Proc. Cambridge Philos. Soc.* **23**, 542 (1926); E. Fermi, *Z. Phys.* **48**, 73 (1928).

[68] C. H. Hodges, *Can. J. Phys.* **51**, 1428 (1973).

[69] W. Ekardt, *Phys. Rev. B* **29**, 1558 (1894).

[70] W. A. De Heer, W. D. Knight, M. Y. Chou, and M. L. Cohen, *Solid State Phys.* **40**,

93 (1987).

[71] R. N. Barnett, U. Landman, and G. Rajagopal, *Phys. Rev. Lett.* **67**, 3058 (1991); see also R. N. Barnett and U. Landman, *ibid.* **69**, 1472 (1992); R. N. Barnett, U. Landman, A. Nitzan, and G. Rajagopal, *J. Chem. Phys.* **94**, 608 (1991); H.-P. Cheng, R. N. Barnett, and U. Landman, *Phys. Rev. B* **48**, 1820 (1993).

[72] U. Röthlisberger and W. Andreoni, *J. Chem. Phys.* **94**, 8129 (1991).

[73] J. P. Perdew and A. Zunger, *Phys. Rev. B* **23**, 5048 (1981).

[74] L. C. Balbás, A. Rubio, and J. A. Alonso, *Chemical Phys.* **120**, 239 (1988).

[75] Z. Penzar and W. Ekardt, *Z. Phys. D* **17**, 69 (1990).

[76] D. M. Wood, *Phys. Rev. Lett.* **46**, 749 (1981).

[77] M. P. J. Van Staveren, H. B. Brom, L. J. de Jongh, and Y. Ishii, *Phys. Rev. B* **35**, 7749 (1987).

[78] J. P. Perdew and Y. Wang, *Phys. Rev. B* **38**, 12228 (1988).

[79] Ph. J. Siemens and A. S. Jensen, *Elements of nuclei* (Addison-Wesley, New York, 1987).

[80] We emphasize that while the effective potentials are significantly different when SIC is used, other quantities, such as the total energy, IPs, and EAs are only slightly altered by SIC as shown in Ref. [73], and by our own calculations.

[81] S. Hofmann, *Proton radioactivity* in *Particle Emission from Nuclei*, D. N. Poenaru and M. S. Ivascu (eds.), (CRC Press, Boca Raton, Florida, 1989) Vol. II, p. 25.

[82] C. Bréchignac, Ph. Cahuzac, F. Carlier, and J. Leygnier, *Phys. Rev. Lett.* **63**, 1368 (1989).

[83] N. Troullier and J. L. Martins, *Phys. Rev. B* **46**, 1754 (1992); J. L. Martins, N. Troullier, and J. H. Weaver, *Chem. Phys. Lett.* **180**, 457 (1991).

[84] J. Kohanoff, W. Andreoni, and M. Parrinello, *Chem. Phys. Lett.* **198**, 472 (1992).

[85] K. Yabana and G. F. Bertsch, *Physica Scripta* **48**, 633 (1993).

[86] N. Van Giai and E. Lipparini, *Z. Phys. D* **27**, 193 (1993).

[87] M. J. Puska and R. M. Nieminen, *Phys. Rev. A* **47**, 1181 (1993).

[88] B. Grammaticos, *Z. Phys. A* **305**, 257 (1982).

[89] G. A. Gallup, *Chem. Phys. Lett.* **187**, 187 (1991).

[90] R. C. Haddon, L. E. Brus, and K. Raghavachari, *Chem. Phys. Lett.* **125**, 459 (1986).

[91] M. Gerloch and R. C. Slade, *Ligand field parameters*, (Cambridge Univ. Press, London, 1973).

[92] A. Rosén and B. Wästberg, *J. Chem. Phys.* **90**, 2525 (1989); B. Wästberg and A. Rosén, *Physica Scripta* **44**, 276 (1991).

[93] L. Ye and A. J. Freeman, *Chem. Phys.* **160**, 415 (1992).

[94] Due to the changing spill-out with excess charge z, the capacitance should be written as $C + \delta(z)$. For our purposes here the small correction $\delta(z)$ can be neglected.

[95] M. R. Pederson and A. A. Quong, *Phys. Rev. B* **46**, 13584 (1992).

[96] Y. Wang, D. Tománek, G. F. Bertsch, and R. S. Ruoff, *Phys. Rev. B* **47**, 6711 (1993).

[97] M. Sai Baba, T. S. Lakshmi Narasimhan, R. Balasubramanian, and C. K. Mathews, *Int. J. Mass Spectrom. Ion Processes* **125**, R1 (1993).

[98] R. L. Hettich, R. N. Compton, and R. H. Ritchie, *Phys. Rev. Lett.* **67**, 1242 (1991).

[99] P. A. Limbach, L. Schweikhard, K. A. Cowen, M. T. McDermott, A. G. Marshall, and J. V. Coe, *J. Am. Chem. Soc.* **113**, 6795 (1991).

[100] For certain systems, such as for example sodium clusters, an orbitally-averaged-like SIC treatment yielded highest-occupied-molecular-orbital (HOMO) energies for anions in adequate agreement with the calculated electron affinities (see Refs. [3, 23]).

[101] J. Cioslowski and K. Raghavachari, *J. Chem. Phys.* **98**, 8734 (1993).

46   *Constantine Yannouleas and Uzi Landman*

[102] A. I. Baz', Y. B. Zel'dovich, and A. M. Perelomov, *Scattering, reactions, and decay in nonrelativistic quantum mechanics*, (Israel Program for Scientific Translations Ltd., Jerusalem, 1969).

[103] V. De Coulon, J. L. Martins, and F. Reuse, *Phys. Rev. B* **45**, 13 671 (1992).

[104] U. Landman, W. D. Luedtke, N. Burnham, and R. J. Colton, *Science* **248**, 454 (1990).

[105] U. Landman, W. D. Luedtke, B. E. Salisbury, and R. .L. Whetten, *Phys. Rev. Lett.* **77**, 1362 (1996).

[106] U. Landman, W. D. Luedtke, and J. Gao, *Langmuir* **12**, 4514 (1996).

[107] E. N. Bogachek, A. M. Zagoskin, and I. O. Kulik, *Fiz. Nizk. Temp.* **16**, 1404 (1990) [*Sov. J. Low Temp. Phys.* **16**, 796 (1990)].

[108] J. I. Pascual, J. Mendez, J. Gomez-Herrero, J. M. Baro, N. Garcia, and V. T. Binh, *Phys. Rev. Lett.* **71**, 1852 (1993).

[109] L. Olesen, E. Laegsgaard, I. Stensgaard, F. Besenbacher, J. Schiotz, P. Stoltze, K. W. Jacobsen, and J. N. Norskov, *Phys. Rev. Lett.* **72**, 2251 (1994).

[110] J. I. Pascual, J. Mendez, J. Gomez-Herrero, J. M. Baro, N. Garcia, U. Landman, W. D. Luedtke, E. N. Bogachek, and H.-P. Cheng, *Science* **267**, 1793 (1995).

[111] D. P. E. Smith, *Science* **269**, 371 (1995).

[112] G. Rubio, N. Agrait, and S. Vieira, *Phys. Rev. Lett.* **76**, 2302 (1996).

[113] A. Stalder and U. Durig, *Appl. Phys. Lett.* **68**, 637 (1996).

[114] J. M. Krans, J. M. van Ruitenbeek, V. V. Fisun, I. K. Yanson, and L. J. de Jongh, *Nature* **375**, 767 (1995).

[115] J. L. Costa-Kramer, N. Garcia, P. Garcia-Mochales, and P. A. Serena, *Surface Science* **342**, 11144 (1995).

[116] R. N. Barnett and U. Landman, *Nature* **387**, 788 (1997).

[117] For an axially symmetric nanowire with variable radius, see Ref. [41].

[118] A. G. Scherbakov, E. N. Bogachek, and U. Landman, *Phys. Rev. B* **53**, 4054 (1996).

[119] E. N. Bogachek, A. G. Scherbakov, and U. Landman, *Phys. Rev. B* **56**, 1065 (1997).

[120] E. N. Bogachek, A. G. Scherbakov, and U. Landman, *Phys. Rev. B* **53**, R13246 (1996).

[121] A. Garcia-Martin, J. A. Torres, and J. J. Saenz, *Phys. Rev. B* **54**, 13448 (1996).

[122] R. A. Gherghescu, D. N. Poenaru, A. Solov'yov, and W. Greiner, *Int. J. Mod. Phys. B* **22**, 4917 (2008).

[123] W. A. Saunders, *Phys. Rev. A* **46**, 7028 (1992).

[124] Here, we consider clusters of monovalent elements (Na, K, and Cu). For polyvalent elements, N in Eq. (A.6) must be replaced by Nv, where v is the valency.

[125] I. S. Gradshteyn and I. M. Ryzhik, *Table of integrals, series, and products*, (Academic, New York, 1980) Ch. 8.11.

[126] R. W. Hasse and W. D. Myers, *Geometrical relationships of macroscopic nuclear physics*, (Springer-Verlag, Berlin, 1988) Ch. 6.5.

[127] S. G. Nilsson, *K. Danske Vidensk. Selsk. Mat.-Fys. Medd.* **29**, No. 16 (1955).

[128] K. L. Clemenger, *Phys. Rev. B* **32**, 1359 (1985).

[129] W. A. Saunders, *Ph.D. dissertation*, University of California, Berkeley (1986); W. A. Saunders, K. Clemenger, W. A. de Heer, and W. D. Knight, *Phys. Rev. B* **32**, 1366 (1985).

[130] K. L. Clemenger, *Ph.D. dissertation*, University of California, Berkeley (1985).

[131] J. R. Nix, *Annu. Rev. Nucl. Part. Sci.* **22**, 65 (1972).

[132] R. K. Bhaduri and C. K. Ross, *Phys. Rev. Lett.* **27**, 606 (1971).

[133] The perturbation $\mathbf{l}^2 - <\mathbf{l}^2>_n$ in the hamiltonian (A.15) influences the shell correction ΔE_{sh}^{Str}, but not the average, $\widetilde{E}_{sp}$, of the single-particle spectrum, since $U_0 = 0$

Shell-correction and orbital-free density-functional methods for finite systems   47

for all shells with principal quantum number n higher than the minimum number required for accomodating N_e electrons (see, Ref. [43], p. 598 ff.).

[134] A. Herlert, L. Schweikhard, and M. Vogel, *Eur. Phys. J. D* **16**, 65 (2001).
[135] J. Maruhn and W. Greiner, *Z. Phys.* **251**, 431 (1972).